Development and evaluation of CO_2 transport in MPAS-A v6.3

Tao Zheng[1], Sha Feng[2], Kenneth J. Davis[2], Sandip Pal[3], and Josep Anton Morguí[4]

[1]Department of Geography & Institute of Great Lake Research, Central Michigan University, Mount Pleasant, MI. USA
[2]Department of Meteorology and Atmospheric Science, The Pennsylvania State University, University Park, PA. USA
[3]Department of Geosciences, Texas Tech University, Lubbock, TX. USA
[4]Environmental Science and Technology Institute, Universitat Autònoma de Barcelona, ICTA-UAB, Bellaterra, Spain

Correspondence to: Tao Zheng (zheng1t@cmich.edu)

Abstract.

Chemistry transport models (CTM) play an important role in understanding fluxes and atmospheric distribution of carbon dioxide (CO_2). They have been widely used for modeling CO_2 transport through forward simulations and inferring fluxes through inversion systems. With the increasing availability of high resolution observations, it has been become possible to estimate CO_2 fluxes at higher spatial resolution. In this work we implemented CO_2 transport in Model Prediction Across Scales-Atmosphere (MPAS-A). The objective is to use the variable-resolution capability of MPAS-A to enable high resolution CO_2 simulation at limited region with a global model. Treating CO_2 as an inert tracer, we implemented in MPAS-A (v6.3) the CO_2 transport processes, including advection, vertical mixing by boundary layer scheme, and convective transport. We first evaluated the newly implemented model's tracer mass conservation and then its CO_2 simulation accuracy. A one-year (2014) MPAS-A simulation is evaluated at the global scale using CO_2 measurements from 50 near-surface stations and 18 Total Carbon Column Observing Network (TCCON) stations. The simulation is also compared with two global models: National Oceanic and Atmospheric Administration (NOAA) CarbonTracker v2019 (CT2019) and European Center for Medium-Range Weather Forecasts (ECMWF) Integrated Forecasting System (IFS). A second set of simulation (2016-2018) is used to evaluate MPAS-A at regional scale using Atmospheric Carbon and Transport-America (ACT-America) aircraft CO_2 measurements over the eastern United States. This simulation is also compared with CT2019 and a 27-km WRF-Chem simulation. The global scale evaluations show that MPAS-A is capable of representing the spatial and temporal CO_2 variation with comparable level of accuracy as IFS of similar horizontal resolution. The regional scale evaluations show that MPAS-A is capable of representing the observed atmospheric CO_2 spatial structures related with the mid-latitude synoptic weather system, including the warm versus cold sector distinction, boundary layer to free troposphere difference, and frontal boundary CO_2 enhancement. MPAS-A's performance in representing these CO_2 spatial structures are comparable with the global model CT2019 and regional model WRF-Chem.

1 Introduction

Carbon dioxide (CO_2) is the most important greenhouse gas, and our knowledge about its sources and sinks still have large gaps. Inversion systems are tools for inferring surface CO_2 fluxes based on observations and chemistry transport models

(CTM). Two types of CTMs are commonly used: global models and regional models. Global models are commonly used for inferring CO_2 fluxes at coarse spatial scales (Patra et al., 2008; Schuh et al., 2019; Jacobson et al., 2007, 2020). With the fast increasing number of atmospheric CO_2 observations, including those acquired by ground based, airborne, and satellite instruments, regional inversion system have been developed and applied to estimate carbon fluxes at higher resolution (Gerbig et al., 2009; Pillai et al., 2012; Lauvaux et al., 2012; Hu et al., 2019; Zheng et al., 2018, 2019).

A major challenge of atmospheric CO_2 inversion modeling is how to partition the model-data mismatch (MDM) among the transport model error, observation error, and prior flux error (Baker et al., 2006). In the Bayesian inversion framework, the error covariance matrix $\mathbf{R}$ is commonly used to represent the combined error of transport model and observations. While it is important to correctly represent the transport model error in an inversion system, it is also important to reduce the error in order to estimate the fluxes with less uncertainty. One approach to reduce the transport model error is to increase the horizontal resolution of a simulation. For instance, Feng et al. (2016) found high-resolution WRF-Chem simulation improved CO_2 model-data comparison because of better resolved planetary boundary layer (PBL) and better representation of spatial variability of CO_2 fluxes. In a recent study, Agusti-Panareda et al. (2019) investigated the impacts of transport model's horizontal resolutions on simulated CO_2 accuracy, and they found that CO_2 variability are generally better represented by higher resolution simulations.

Global high resolution CO_2 simulations require large computational resources. Regional (limited area) models, which have lower computational cost than their global model counterpart at the same horizontal resolution, are often used for high resolution CO_2 transport (Feng et al., 2016; Diaz-Isaac et al., 2019, 2018) and inverse modeling (Sarrat et al., 2007; Gerbig et al., 2008; Lauvaux et al., 2012; Zheng et al., 2019). However a regional model requires CO_2 transported from outside its model domain to be prescribed. For a CO_2 inversion system, having lateral boundaries increase the size of the control vector to be optimized (Rayner et al., 2019). A number of approaches have been applied to the CO_2 lateral boundary problem, such as assuming the boundary inflow is perfectly known (Gockede et al., 2010), correcting the lateral boundary condition using observation prior to inversion (Lauvaux et al., 2012; Schuh et al., 2013), or jointly optimizing flux and lateral boundary condition (Zheng et al., 2018). When CO_2 lateral boundary is optimized, an inversion system adjusts its CO_2 fields at the boundary prescribed by a parent global model in addition to adjusting surface fluxes. This could be problematic for inversion systems that use satellite derived column averaged CO_2 measurements (XCO_2) because model-data mismatches in the free troposphere (FT) are often originated from outside a regional model's limited area domain (Feng et al., 2019; Lauvaux and Davis, 2014).

The objective of the present paper is to provide an alternative high-resolution CO_2 transport modeling approach to regional transport models. This approach is to use a global variable-resolution model which allows for local grid refinement that enables high resolution simulation over an interested region without incurring the prohibitively high computational cost or the lateral boundary condition. Variable-resolution through local grid refinement has been widely used in Numerical Weather Prediction (NWP) models, such as MPAS-A (Skamarock et al., 2012), Ocean-Land-Atmosphere Model (OLAM) (Walko and Avissar, 2008a, b), Energy Exascale Earth System Model (E3SM) (Golaz et al., 2019), and Finite-Volume Cubed-Sphere model(FV3)

(Putman and Lin, 2007). One benefit of local mesh refinement is enabling regional high-resolution modeling without incurring the lateral boundary condition and its associated problems, such as solution mismatches between the driving global model and the evolving regional model (Davies, 2014). Model Prediction Across Scales-Atmosphere (MPAS-A) is a fully compressible non-hydrostatic global atmospheric model which uses finite-volume numeric solver discretized on centroidal Voronoi mesh with C-grid staggering of its prognostic variables (Skamarock et al., 2012; Thuburn, 2007; Ringler et al., 2010). The centroidal Voronoi mesh allows for local refinement and variable-resolution horizontal mesh which can be gradually changed from coarse to fine resolutions (Skamarock et al., 2012; Ringler et al., 2008).

To enable CO_2 transport modeling, we implemented atmospheric CO_2 transport processes, including advection, vertical mixing by PBL scheme, and convective transport in MPAS-A v6.3. Because the CO_2 transport processes are fully integrated into the model's meteorological time steps, the resulting MPAS-A CO_2 is an online CTM. We used the newly developed model to conduct two sets of simulations over a 60-15 km variable-resolution global domain. Then the simulation results are evaluated using an extensive set of airborne observations over the eastern United States and near-surface observations from surface and tower stations across the globe. The simulation accuracy of MPAS-A is compared with three established CO_2 modeling systems based on the same observational data: WRF-Chem (Skamarock et al., 2008; Feng et al., 2019), Carbontracker (v2019, CT2019 hereafter) (Jacobson et al., 2020), and ECWMF IFS (Agusti-Panareda et al., 2014, 2019).

2 Implementation of CO_2 transport in MPAS-A

This section describes the major modifications to MPAS-A that we made to implement CO_2 tracer transport. We represent CO_2 by its dry air mixing ratio (q_{co_2}) and model its atmospheric transport by adding its continuity equation in MPAS-A following Eq. 7 of Skamarock et al. (2012).

$$\frac{\partial(\tilde{\rho}\, q_{co_2})}{\partial t} = -(\nabla \cdot \tilde{\rho}\, q_{co_2}\, \mathbf{V})_\zeta + F_{bl} + F_{cu} \tag{1}$$

where $\tilde{\rho} = \rho_d/(\partial\zeta/\partial z)$, ρ_d is dry air density, ζ is the vertical coordinate, z is geometric height, t is time, and $\mathbf{V}$ is the velocity vector. The left hand side of the equation is the total CO_2 time tendency ($\partial(\tilde{\rho}\ \mathrm{q}_{co_2})/\partial t$), and the first, second, and third terms on the right hand side represent the contributions from advection, vertical mixing, and convective transport respectively. CO_2 tendency from advection is modeled in flux form (Section 2.1), while tendency from vertical mixing (F_{bl}) and convective transport (F_{cu}) are modeled in uncoupled form ($\partial q_{co_2}/\partial t$) which are coupled to $\tilde{\rho}$ before being added to the total tendency. We choose to implement CO_2 vertical mixing in the Yonsei University (YSU) PBL scheme (Hong et al., 2006), and CO_2 convective transport in Kain-Fritsch (KF) scheme (Kain, 2004) because they are widely used in CTM and have been validated using observations (Borge et al., 2008; Hu et al., 2010; Kretschmer et al., 2012; Polavarapu et al., 2016). Details of

the three terms on the right hand side of Eq. 1 are described in the following sections. We note that because the monotonicity constraint in the third-order scalar horizontal advection scheme (Skamarock and Gassmann, 2011) introduces dissipation MPAS-A does not use any explicit horizontal diffusion for scalar. Accordingly we did not include horizontal diffusion for CO_2.

2.1 CO_2 advection

Advection is the most significant component of CO_2 atmospheric transport. Following the example of other scalars in MPAS-A (Skamarock and Gassmann, 2011), we model CO_2 advection as:

$$(\nabla \cdot \tilde{\rho} q_{co_2} \mathbf{V})_\zeta = \big[\frac{\partial(\tilde{\rho} u q_{co_2})}{\partial x} + \frac{\partial(\tilde{\rho} v q_{co_2})}{\partial y}\big]_\zeta + \frac{\partial(\tilde{\rho} w q_{co_2})}{\partial \zeta} \tag{2}$$

where $\mathbf{V} = (u, v, w)$, and u, v, and w is the zonal, meridional, and vertical wind respectively. The first item on the right hand side enclosed in the square bracket is the CO_2 horizontal flux divergence, and second item is the vertical flux divergence. The horizontal flux divergence is transformed via the divergence theorem into an integral of flux over each control volume, which is modeled as:

$$\big[\frac{\partial(\tilde{\rho} u q_{co_2})}{\partial x} + \frac{\partial(\tilde{\rho} v q_{co_2})}{\partial y}\big]_\zeta = \frac{1}{A_i} \sum_e^{n_e} l_e F_e(\mathbf{V}_H, \tilde{\rho} q_{co_2}) \tag{3}$$

where e indexes the edges of a cell and n_e represents the number of edges the cell has, l_e is the length of an edge, A_i is the cell's areal size, $F_e(\mathbf{v}_H, \tilde{\rho} q_{co_2})$ is the instantaneous horizontal CO_2 flux that crosses the cell edge e, and $\mathbf{V}_H = (u, v)$ is the horizontal wind vector. The details of MPAS-A instantaneous horizontal flux calculation can found in Skamarock and Gassmann (2011). The vertical CO_2 flux divergence in Eq. 2 is calculated using finite difference

$$\frac{\partial(\tilde{\rho} w q_{co_2})}{\partial \zeta} = \frac{1}{\Delta \zeta} \big[F(w, \tilde{\rho} q_{co_2})_{k+\frac{1}{2}} - F(w, \tilde{\rho} q_{co_2})_{k-\frac{1}{2}}\big] \tag{4}$$

where $F(w, \tilde{\rho} q_{co_2})$ is the vertical CO_2 flux that crosses a cell's vertical face, and k indexes the vertical coordinate.

2.2 CO_2 vertical mixing

Like in WRF (Skamarock et al., 2008), a PBL parameterization in MPAS-A treats the vertical mixing of momentum and scalars not only in the boundary layer (BL) but in the entire atmospheric column. YSU (Hong et al., 2006) is one of the PBL schemes available in MPAS-A 6.3. The present YSU scheme treats vertical mixing of momentum, potential temperature, and water species, but not atmospheric tracers. We modified the scheme to treat CO_2 vertical mixing.

In the YSU scheme, after the top of BL is determined, the vertical mixing of momentum, potential temperature, and water vapor are treated separately: above BL, local K-profile approach (Louis, 1979) is used for vertical diffusion of momentum and

scalars (Noh et al., 2003; Hong et al., 2006). Within BL, an entrainment flux at the inversion layer is included for momentum and scalars diffusion. In addition, a countergradient mixing term is included for the diffusion of momentum and potential temperature to account for the convective-driven mixing (γ_c of Eq. 4 in Hong et al. (2006)), but this term is not used for water vapor.

Following the treatment of water vapor, we parameterize CO_2 vertical mixing in BL as

$$\frac{\partial q_{co_2}}{\partial t} = \frac{\partial}{\partial z}\left[K_h(\frac{\partial q_{co_2}}{\partial z}) - \overline{(w'q'_{co_2})_h}(\frac{z}{h})^3\right] \tag{5}$$

where z is the vertical distance to surface, h is BL top height, K_h is vertical eddy diffusivity. Note that this formulation does not include a countergradient mixing term following the treatment of water vapor in the original YSU (Hong et al., 2006). The second term in the square bracket of Eq. 5 represents the contribution from CO_2 entrainment flux at the inversion layer, which is parameterized as:

$$\overline{(w'q'_{co_2})_h} = w_e \Delta q_{co_2}|_h \tag{6}$$

where $\Delta q_{co_2}|_h$ is the CO_2 mixing ratio difference across the inversion layer, and w_e is the entrainment rate at the inversion layer calculated by Eq. A11 of Hong et al. (2006). Above BL top, vertical mixing of CO_2 is parameterized as:

$$\frac{\partial q_{co_2}}{\partial t} = \frac{\partial}{\partial z}\left[K_h(\frac{\partial q_{co_2}}{\partial z})\right] \tag{7}$$

We use the same value for CO_2 vertical diffusivity as water vapor. The details of K_h calculation can be found in the appendix of Hong et al. (2006), and its value is limited between 0.01 and 1000 $\mathrm{m^2 s^{-1}}$ to prevent too weak or strong vertical mixing. The term $\partial q_{co_2}/\partial t$ from Eqs. 5 is coupled with dry air density before being applied to the continuity equation (Eq. 1).

2.3 CO_2 convective transport

For convective transport, we modified the Kain-Fritsch scheme (hereafter KF) (Kain, 2004) to include the CO_2 treatment. KF is a mass-flux convection scheme which rearranges mass in an air column using convective updrafts, downdrafts, and environmental mass fluxes. Both the updraft and downdraft entrain from and detrain to the environment, thus altering the vertical profile of an air column's thermodynamic properties. We added the CO_2 convective transport as:

$$\frac{\partial q_{co_2}}{\partial t} = \frac{(M_u + M_d)}{\rho A}\frac{\partial q_{co_2}}{\partial z} + \frac{M_{ud}}{M}(q^u_{co_2} - q_{co_2}) + \frac{M_{dd}}{M}(q^d_{co_2} - q_{co_2}) \tag{8}$$

where q_{co_2}, $q^u_{co_2}$, and $q^d_{co_2}$ are the CO_2 mixing ratio in the environment, updraft, and downdraft respectively, M_u and M_d are the updraft and downdraft mass respectively, ρ is the environment air density, A is the horizontal area of a cell, $M = \rho A \delta z$ is the mass of environmental air in a grid box, and M_{ud} and M_{dd} are the detrainment from the updraft and downdraft respectively.

In KF, the updraft and downdraft mass and the rates for the entrainment and detrainment are determined by a steady-state plume model and a convective available potential energy (CAPE) closure assumption: 90% of the existing CAPE should be removed by the convection parameterization (Kain and Fritsch, 1990; Fritsch and Chappell, 1980; Kain, 2004). Because the calculation of the updraft and downdraft mass fluxes is related to a cell's horizontal area, the KF scheme may behave differently at different areas of MPAS-A's variable-resolution grid. The updraft source layers are determined by a search from the model's lowest vertical level for a group of consecutive layers that is buoyant and at least 50 hPa deep (Kain, 2004). The initial value of CO_2 mixing ratio in the updraft is modeled as a pressure weighted average of the source layers:

$$q^u_{co_2} = \sum_k \frac{\delta q_{co_2,k}\, \delta p_k}{\delta p_k} \tag{9}$$

where δp_k is layer's pressure depth, and $q_{co_2,k}$ is the layer's CO_2 mixing ratio. CO_2 mixing ratio of the updraft is modified by the entrainment of the environmental air through its ascent from its starting level to the cloud top.

$$q^u_{co_2} = \frac{q^u_{co_2} M_u + q_{co_2} M_{ue}}{M_u + M_{ue}} \tag{10}$$

where M_{ue} is the updraft entrainment. The initial CO_2 mixing ratio of a downdraft (q^d_{co2}) is the same as that of the environment (q_{co2}) at the downdraft starting level and it is modified by entrainment through the downdraft descent:

$$q^d_{co_2} = \frac{q^d_{co_2} M_d + q_{co_2} M_{de}}{M_d + M_{de}} \tag{11}$$

where M_{de} is the downdraft entrainment.

3 Model evaluation

In this section we evaluate the newly developed MPAS-A CO_2 transport model through simulation experiments. After describing the simulation configuration (Sect. 3.1), we assess the model's global mass conservation property (Sect. 3.2). Then we evaluate the model's CO_2 transport accuracy at the global scale using hourly near-surface CO_2 observations from 50 in situ stations and column-averaged CO_2 dry air mole fraction (XCO_2) measurements from 18 Total Carbon Column Observing Network (TCCON) stations (Sect. 3.3). Finally, we evaluate MPAS-A at the regional scale using high-resolution airborne measurements from ACT over the eastern United States (Sect. 3.4). MPAS-A CO_2 transport are also compared with three established CTMs: NOAA CT2019 (Jacobson et al., 2020), ECMWF IFS (Agusti-Panareda et al., 2019), and WRF-Chem (Skamarock et al., 2008). In the following model evaluation, we use root mean square error (RMSE), bias (μ), and random error (STDE) as the model accuracy metrics:

$$\text{RMSE} = \sqrt{\frac{1}{N}\sum_{i=1}^{N}(m_i - o_i)^2} \tag{12}$$

$$\mu = \frac{1}{N}\sum_{i=1}^{N}(m_i - o_i) \tag{13}$$

$$\text{STDE} = \sqrt{\frac{1}{N}\sum_{i=1}^{N}(m_i - o_i - \mu)^2} \tag{14}$$

where o_i and m_i represent the observed and modeled values respectively.

For model-data intercomparison, MPAS-A model data need to be interpolated to the observation space. Following Patra et al. (2008), the model is sampled in the horizontal by taking the nearest cell overland. MPAS-A uses a height-based terrrain-following vertical coordinate (Skamarock et al., 2012). At a given cell, the height of the k^{th} vertical layer boundary is denoted as z_k^h. The height of the layer center is $z_k = 0.5 \times (z_k^h + z_{k+1}^h)$. In MPAS-A, horizontal wind fields are defined at the vertical layer boundaries and CO_2 fields are defined at layer centers. For horizontal wind fields validation using radiosonde data (Sect. 3.3.1), the column profile of air pressure and horizontal wind fields defined at layer boundaries are used to interpolate to the measurements' pressure levels. For comparison with near-surface CO_2 observations from in-situ stations (Sect. 3.3.3) and aircraft observations (Sect. 3.4), model CO_2 defined at layer centers are interpolated to the measurement heights. Vertical interpolation and integration for the comparison with TCCON XCO_2 are described in Sect. 3.3.4. MPAS-A simulation outputs are saved at 1-hour intervals. For comparison with radiosonde observations and near-surface CO_2 observations, no temporal interpolations are applied: observations are paired with the closest hourly MPAS-A output. For comparison with aircraft observations, the hourly model outputs that bracket an observation's time stamp are used for the temporal interpolation.

3.1 Simulation experiment configuration

For all subsequent simulations, MPAS-A uses a 60-15km variable-resolution global mesh. Fig. 1 shows the cell size (in km^2) of the simulation domain, where the highest resolution (15 km) over North America has cell size smaller than 250 km^2 which gradually increases to about 3,600 km^2 for the rest of the global domain. On the vertical direction, there are 55 levels spanning from surface to 30 km above the mean sea level. Model time step is 90 seconds in accordance with the highest (15km) horizontal resolution. For physical parameterizations, in addition to the modified YSU PBL (Hong et al., 2004) and Kain-Fristch cumulus schemes (Kain, 2004) described in Section 2, we use RRTMG for longwave and shortwave radiation (Iacono et al., 2008), Noah land scheme (Chen and Dudhia, 2001), Monin-Obukhov surface layer scheme, and WRF single-moment 6-class microphysics scheme (Hong and Lim, 2006). The third-order accuracy advection is used for all scalars and CO_2 tracer. A summary of the physics parameterizations used in the simulations is given in Table 1.

Initial meteorological fields are generated from the ERA-Interim reanalysis (Dee et al., 2011). To keep model meteorological fields close to the reanalysis, MPAS-A meteorological fields are re-initialized using the analysis at 00:00 UTC each day throughout a simulation period. CO_2 mixing ratio is kept unchanged during the meteorology re-initializations, thus a free-running simulation. This configuration is the same as that used by Agusti-Panareda et al. (2014, 2019) in their IFS global CO_2 simulations. The first CO_2 initial condition for a simulation is from CT2019 $3^\circ \times 2^\circ$ posterior dry mole fraction product and surface CO_2 fluxes are prepared by interpolating the CT2019 3-hourly $1^\circ \times 1^\circ$ posterior flux product (Jacobson et al., 2020). The four CT2019 fluxes (biosphere, ocean, fossil fuel, and fire) are interpolated to MPAS-A model grid and ingested at 3-hour intervals throughout a simulation.

3.2 CO_2 mass conservation

For CTM, it is very important to maintain the global CO_2 mass conservation (Agusti-Panareda et al., 2017; Polavarapu et al., 2016). Because meteorological re-initializations introduce changes in dry air mass, they impact MPAS-A's global CO_2 mass conservation. We first examine MPAS-A's inherent mass conservation property through a simulation without the meteorological re-initializations in Sect. 3.2.1. Then we examine and treat the impacts of the meteorological re-initializations in Sect. 3.2.2.

3.2.1 Mass conservation without meteorology re-initialization

To examine MPAS-A's mass conservation property, we conducted a MPAS-A simulation that lasts from January 1 to December 31 2014. The simulation is initialized with the CT2019 CO_2 mole fraction and is driven with 3-hourly CT2019 surface CO_2 fluxes. Meteorological re-initializations are not applied during the simulation and the model outputs are saved using double-precision. MPAS-A's global dry air mass (M_{air}) is then calculated at 00:00 UTC each day through the one-year simulation using Eq. 15,

$$\mathrm{M_{air}} = \sum_{k}^{L} (\sum_{i}^{N} A_i \, h_{i,k} \, \rho_{i,k}) \tag{15}$$

where subscript i indexes the horizontal cell, subscript k indexes the vertical level, A_i is cell size, $h_{i,k}$ is cell height, and $\rho_{i,k}$ is dry air density ($\mathrm{kg\,m^{-3}}$). After the model's global dry air mass is calculated at 00:00 UTC each day of the simulation period, its variation is quantified as a ratio $E^t_{air} = (M^t_{air} - M^0_{air})/M^0_{air}$, where M^0_{air} and M^t_{air} are the model's global dry air mass at the simulation start (00:00 UTC January 1 2014) and the current time step respectively. The top panel of Fig. 2 shows E^t_{air} at 00:00 UTC of each day through the one-year simulation period. The figure shows that the maximal magnitude of E^t_{air} is less than 4×10^{-12} during the one-year simulation. In comparison, the total dry air mass of ECMWF IFS increases about 0.01% of its initial value in a 10-day forecast (Diamantakis and Flemming, 2014). Similarly, the Environment and Climate Change Canada (ECCC) Global Environmental Multiscale (GEM) model loses about 0.01% of its initial total dry air mass in a 10-day forecast (Polavarapu et al., 2016). MPAS-A has a significantly lower global dry air mass variation than the two global models

because its explicit grid point advection scheme conserves mass (Skamarock and Gassmann, 2011) while the semi-Lagrangian advection scheme used by IFS and GEM does not conserves mass (Williamson, 1990). Thus, no mass fixer (Diamantakis and Flemming, 2014; Polavarapu et al., 2016) is used in MPAS-A.

MPAS-A's global CO_2 mass (M_{co_2}) is calculated using Eq. 16,

$$M_{co_2} = \sum_{k}^{L}(\sum_{i}^{N} A_i\, h_{i,k}\, \rho_{i,k}\, q_{i,k}) \tag{16}$$

where $q_{i,k}$ is CO_2 dry air mixing ratio ($\mathrm{kg/kg}$) and the rest of the terms are the same as in Eq. 15. To assess the global CO_2 mass conservation, M_{co_2} calculated using Eq. 16 is adjusted for the CO_2 mass introduced through the ingestion of the 3-hourly surface CO_2 fluxes. For a 3-hour period, total CO_2 mass introduced through the surface CO_2 fluxes is $\sum_i^N A_i\, F_i\, \Delta t$, where F_i is the combined biosphere, ocean, fossil fuel, and fire CO_2 fluxes ($\mathrm{kg\,m^{-2}\,s^{-1}}$) at a surface cell, A_i is the cell's areal size, N is number of surface cell, and Δt=3 hours. After the adjustment, the variation of global mass of CO_2 is quantified as a ratio, $E^t_{co_2} = (M^t_{co_2} - M^0_{co_2})/M^0_{co_2}$, where $M^0_{co_2}$ and M^t_{co2} are the model's initial and current time step global CO_2 mass. $E^t_{co_2}$ at 00:00 UTC of each day of the simulation period is shown in the lower panel of Fig. 2. The figure shows that the maximal magnitude of $E^t_{co_2}$ is about 10^{-5}. This is much higher compared to E^t_{air} and it is due to the strong gradients caused by surface CO_2 flux which challenge the model's numerical scheme.

3.2.2 CO_2 mass conservation during meteorology re-initialization

When meteorological re-initialization is applied during a simulation, the values of dry air density in MPAS-A are replaced by values from the initialization files generated from the ERA-Interim reanalysis. In most cases, this will cause dry air density change which in turn will introduce CO_2 mass change if CO_2 dry air mixing ratios are kept unchanged during the re-initialization. To assess this possible change in global CO_2 mass, we conducted another one-year long MPAS-A simulation identical to that used in Section 3.2.1 except that meteorological re-initialization is applied at 24-hour intervals during the simulation. The variation of global CO_2 mass caused by a meteorological re-initialization is quantified as a ratio $E = (M'_{co_2} - M_{co_2})/M_{co_2}$, where M_{co_2} and M'_{co_2} are the global CO_2 mass before and after a meteorological re-initialization. The top panel of Fig. 3 shows the value of E at each meteorological re-initialization. The figure indicates that a meteorological re-initialization could cause a change of more than 0.01% of the global CO_2 mass.

To restore the CO_2 mass conservation after a meteorological re-initialization, we adjust MPA-A's CO_2 fields by a spatially uniform scaling factor: $q'_{i,k} = r \times q_{i,k}$, where $q_{i,k}$ and $q'_{i,k}$ are the CO_2 dry air mixing ratio, before and after the adjustment, respectively. The scaling factor r is calculated as,

$$r = \frac{\sum_k^L(\sum_i^N A_i\, h_{i,k}\, \rho_{i,k}\, q_{i,k})}{\sum_k^L(\sum_i^N A_i\, h_{i,k}\, \rho'_{i,k}\, q_{i,k})} \tag{17}$$

where the notations are the same as in Eq. 16 except that $\rho'_{i,k}$ is the dry air density after a meteorology re-initialization and $\rho_{i,k}$ is the value before the re-initialization. To test the effectiveness of this scaling method, the one-year MPAS-A simulation with meteorological re-initialization was conducted again but this time with the CO_2 dry air mixing ratio adjustment applied after each meteorological re-initialization. The resulting variation in total CO_2 mass is plotted in the lower panel of Fig 3. The figure shows the maximal magnitude of the variation caused by a meteorological re-initialization has been reduced from $\sim 10^{-4}$ to $\sim 10^{-6}$ of the global CO_2 mass. Note the different scales in the y-axis used in the top and bottom panels of Fig. 3.

An alternative approach to restore mass conservation is to scale CO_2 mixing ratio at each grid box individually by

$$q'_{i,k} = \frac{\rho_{i,k}}{\rho'_{i,k}} \times q_{i,k} \tag{18}$$

where notation is the same as Eq. 17. This scaling approach can maintain global CO_2 mass conservation as allowed by machine precision but it will introduce artificial spatial variations in CO_2 mixing ratio. In the simulations in the following sections, we chose to use the first scaling approach to avoid the artificial CO_2 mixing ratio variation by accepting the small changes in global CO_2 mass.

3.3 Model evaluation at global scale

In this section, we evaluate the MPAS-A $\mathrm{CO2}$ transport at the global scale. For the model evaluation, MPAS-A was initialized at 00:00 UTC July 1 2013 and ran till December 31 2014. The model configuration for this simulation is as described in Sect. 3.1. With the first six-month as model spin-up, we use the one-year simulation of 2014 for the model evaluation. First MPAS-A simulated horizontal wind fields are evaluated using radiosonde measurements from 457 stations. Then the model's CO_2 fields are compared with CT2019, near-surface $CO2_2$ measurements from 50 stations, and XCO2 retrievals from 18 TCCON stations.

3.3.1 Evaluation of horizontal wind fields

Accurate meteorological fields are critical for an accurate $\mathrm{CO_2}$ transport simulation. Before evaluating the simulated $\mathrm{CO_2}$, we first evaluate the MPAS-A simulated horizontal wind fields considering their importance in $\mathrm{CO_2}$ advection. We compare MPAS-A simulated horizontal wind fields at 12:00 and 00:00 UTC each day of the simulation period with raidosonde observations from 457 stations located around the globe at four pressure levels:1000, 850, 500, 850, and 200 hPa. Note that because of the 24-hourly meteorological re-initialization, the 00:00 and 12:00 UTC simulation results are 12-hour and 24-hour forecasts respectively. The locations of the 457 radiosonde stations are shown in Fig. S1 of the supplement.

To compare with the similar validation results reported in Agusti-Panareda et al. (2019), the horizontal wind fields evaluation results for January and July of 2014 are listed in Table 2. The table shows that while the mean difference in wind direction decreases with altitude, the mean RMSE vector wind generally increases with altitude, which agree with the IFS validation

results (Agusti-Panareda et al., 2019). At 1000 hPa level, MPAS-A has a slightly lower accuracy than IFS during the same time period. For instance, MPAS-A's mean RMSE vector wind at 1000 hPa is 3.83 m/s for January 2014, and IFS results range from 3.2 m/s to 3.75 m/s for its 9 km and 80 km horizontal resolution simulations. For July 2014, the mean RMSE vector wind at 1000 hPa is 3.47 m/s from MPAS-A and 3.0 m/s to 3.6 m/s for the IFS 9 km and 80 km simulations. At upper level, MPAS-A has a slightly higher accuracy than IFS: at 500 hPa, MPAS-A mean RMSE vector wind is 3.72 m/s and 3.39 m/s for January and July of 2014 respectively, while IFS results in 4.0-4.1 m/s and 3.5-3.6 m/s for the same time period.

An important finding of Agusti-Panareda et al. (2019) is that higher horizontal resolution generally lead to higher meteorological and CO_2 simulation accuracy. To examine the influence of horizontal resolution on MPAS-A's meteorological simulation accuracy, we conducted an additional set of simulation using the identical configuration except that it uses a global 60 km uniform-resolution grid instead of the 60-15 km variable-resolution grid (Fig. 1). Out of the 475 radiosonde stations, 131 are located at 15 km cells in the 60-15 km variable-resolution simulation. These 131 radiosonde stations are all located at 60 km cells in the 60 km uniform-resolution simulation. In Table 3, we calculated and compared horizontal wind accuracy at these 131 radiosonde stations between the 60 km uniform-resolution simulation (labeled as 60 km) and the 60-15 km variable-resolution simulation (labeled as 15 km). The table shows that the horizontal wind fields at these 131 stations are simulated with considerably higher accuracy on the 15 km grid than its 60 km grid counterpart. For instance at 1000 hPa, the mean RMSE wind vector for January 2014 is 3.46 m/s and 3.98 m/s at the 15 km and 60 km grids respectively. The values are 3.10 m/s and 3.64 m/s for July 2014. Table 3 also shows that the difference in the mean RMSE wind vector between the 15 km and 60 km grids is larger near the surface at 850 and 1000 hPa than in the middle and upper troposphere (500 and 200 hPa), which is consistent with the findings of Agusti-Panareda et al. (2019). For both January and July at the four pressure levels, the mean RMSE wind vector at the 131 radiosonde stations at MPAS-A's 15 km grid is either similar to or slightly lower than the mean RMSE wind vector of the around 400 stations from the IFS 9 km resolution simulation (Agusti-Panareda et al., 2019).

3.3.2 Comparison of CO_2 fields with CarbonTracker

Having established that the horizontal wind fields simulated by MPAS-A are sufficiently accurate, the CO_2 fields can be evaluated. First we directly compare XCO_2 from MPAS-A and CT2019 field at the grid scale. First, XCO_2 are calculated at the native grid for MPAS-A (60-15km) and CT2019 ($3^\circ \times 2^\circ$). XCO_2 at a given model cell is calculated as the pressure weighted CO_2 dry air mixing ratio.

$$XCO_2 = (\sum_{k=1}^{N} p_k q_k^{co_2})/(\sum_{k=1}^{N} p_k) \tag{19}$$

where p_k is modeled air pressure at layer k corrected for water vapor, $q_k^{co_2}$ is CO_2 dry air mole fraction at the same level. N is the number of vertical levels in a model. Then, XCO_2 from MPAS-A and CT2019 are regridded from their respective grids an identical $1 \times 1^\circ$ grid for a direct comparison. Figure 4 shows the comparison of XCO_2 from MPAS-A (top) and CT2019

(middle) and their difference (bottom) for July 1 and December 1 2014 at 00:00 UTC. The figure shows that XCO_2 from MPAS-A and CT2019 are generally consistent at the large scales, but differences exist at small spatial scales. The higher horizontal resolution of MPAS-A is evident particularly in July over the northeast and southern China. In December, MPAS-A has higher XCO_2 than CT2019 within the Arctic Circle and southern China. Overall the differences between MPAS-A and CT2019 are evident. The magnitude of differences are mostly within 3 ppm, which is similar to the magnitude reported in Polavarapu et al. (2016) for the GEM model. The differences between MPAS-A and CT2019 are expected due to the differences in the two models' horizontal resolution, dynamics, and physical parameterizations. Because no CTM can be expected to have perfect transport, the acceptability of transport is generally judged through comparisons of model simulation with measurements.

3.3.3 Comparison with near-surface CO_2 measurements

This section compares MPAS-A simulated CO_2 with hourly measurements from 50 stations that were used for the IFS model evaluation in Agusti-Panareda et al. (2019). The information of the 50 stations, including location, elevation, intake height, reference, and type is listed Table 4. Like in Agusti-Panareda et al. (2019), only the highest intake level is used at towers that have multiple intake heights. When multiple observations within an hour are available (such as those with 30-min or shorter time interval), they are averaged to yield a single hourly value. For a given station this results in 744 (24×31) hourly measurements per month at the maximum.

The MPAS-A hourly CO_2 statistics, including RMSE, STDE, and bias at the 50 stations are listed in Tables S1 and S2 of the supplement for January and July of 2014 respectively. For comparison, Tables S1 and S2 also include the statistics from the IFS 9 km and 80 km resolution simulations (Agusti-Panareda et al., 2019) at the same sites for the same time periods. Table S1 shows that RMSE of the MPAS-A simulated hourly CO_2 ranges from 0.17 ppm at the SPO station to 16.65 ppm at the KAS station. In comparison, the IFS simulations also resulted in a much lower RMSE at the SPO than KAS, the latter of which has a RMSE of 4.44 ppm from the 9 km resolution simulation and 10.71 ppm from the 80 km simulation.

The comparison of RMSE and STDE from MPAS-A and IFS are show in Figs 5 and 6 for January and July of 2014, respectively. Table 5 provides a quantitative summary of the hourly CO_2 RMSE between MPAS-A and the IFS 9 km and 80 km simulations. The table shows that for January 2014, the mean RMSE at the 50 stations is 4.20 ppm from MPAS-A, which is higher than IFS 9 km simulation (3.12 ppm, $p = 0.01$) and similar to the IFS 80 km simulation (4.94 ppm, $p = 0.25$). For July 2014, the mean RMSE at the 50 stations is 8.09 ppm from MPAS-A, which is similar to IFS 9 km simulation (8.04, $p = 0.95$) and lower than the IFS 80 km simulation (11.77 ppm, $p = 0.04$). The above comparisons indicate that the 60-15 km MPAS-A simulation has a accuracy level between the IFS 9 km and 80 km simulations.

Agusti-Panareda et al. (2019) found that atmospheric CO_2 transport is generally better represented at higher horizontal resolutions, and mountain stations display the largest improvement at higher resolution as they directly benefit from the more

realistic orography. There are 12 mountain stations of the 50 stations used for the model validation. Table 6 lists the 12 mountain stations in two groups: the first group includes the six mountain stations located at the 15 km cells of the MPAS-A's 60-15 km variable-resolution grid, and the second group includes the other six stations that are located at the 60 km cells of the grid. The table lists the hourly CO_2 RMSE for each of the 12 stations from MPAS-A and IFS 9 km and 80 km simulations are listed for January and July 2014. The table shows that at each of the six mountain stations located at 15 km cells, MPAS-A has lower hourly CO_2 RMSE than the IFS 9 km simulation for July 2014. For January 2014, MPAS-A has lower RMSE than IFS 9 km simulation at five out the six stations (the exception is NWR). In comparison, at the six mountain stations located at its 60 km cells, MPAS-A has higher hourly CO_2 RMSE than IFS 9 km simulation for both January and July of 2014 with the exception of JFJ for July 2014.

3.3.4 Comparison with TCCON XCO_2 measurements

After the comparison with the near-surface CO_2 in the last section, we evaluate MPAS-A CO_2 fields using XCO_2 measurements from 18 TCCON sites listed in Table 7. To compare with TCCON retrieved XCO_2, smoothed MPAS-A XCO_2 is calculated following Wunch et al. (2010):

$$X_{CO_2}^{model} = c_a + \mathbf{h}^T \mathbf{a}^T (\mathbf{x}_m - \mathbf{x}_a) \tag{20}$$

where $X_{CO_2}^{model}$ is the smoothed MPAS-A XCO_2, c_a is the a priori total column, $\mathbf{a}^T$ is TCCON column averaging kernel, $\mathbf{h}^T$ is a dry-pressure weighting function, $\mathbf{x}_m$ is MPAS-A CO_2 dry mole fraction profile, $\mathbf{x}_a$ is the a priori CO_2 dry mole fraction profile. The column profile of CO_2, air pressure, and water vapor mixing ratio extracted from MPAS-A hourly output are interpolated to the same vertical grid as $\mathbf{x}_a$, and dry-pressure weighting function $\mathbf{h}^T$ is calculated following O'Dell et al. (2012) and Eq. A7 of Agusti-Panareda et al. (2014).

At a given TCCON site, averaged hourly XCO_2 (denoted as $X_{CO_2}^{TCCON}$) is calculated as the mean value of all valid XCO_2 retrievals within the hour. $X_{CO_2}^{TCCON}$ are then matched with the calculated hourly XCO2 from MPAS-A (denoted as $X_{CO_2}^{model}$). The comparisons of $X_{CO_2}^{model}$ and $X_{CO_2}^{TCCON}$ at the 18 TCCON sites for the year of 2014 are shown in Fig. 7. The results indicate that the observed seasonal variation in TCCON XCO_2 are in general well represented by MPAS-A. The hourly average XCO_2 comparison between MPAS-A and TCCON are summarized in Table 8. In the table N is the number of data pairs used for calculating the statistics, including RMSE, bias, and correlation coefficient R. The mean RMSE of the 18 sites is 1.35 ppm, which is comparable to the IFS simulations (1.02 to 1.25 ppm) Agusti-Panareda et al. (2019). We then calculated the average daily XCO_2 as the mean value of all the hourly XCO_2 within a given day. The statistics of comparison of daily XCO_2 between MPAS-A and TCCON are also included in Table 8. In the table N is the number of average daily XCO_2 used for calculating the statistics. Compared to their hourly counterparts, the average daily XCO_2 has lower RMSE and higher correlation coefficient.

The mean value of the average daily XCO_2 RMSE of the 18 TCCON sites is 1.23 ppm, which is comparable to IFS simulations (0.97 to 1.25 ppm) reported in Agusti-Panareda et al. (2019).

3.4 Model evaluation at regional scale

In this section, we present an evaluation of the MPAS-A CO_2 simulation accuracy using an extensive high resolution CO_2 observation data acquired through the ACT aircraft campaigns. ACT is a National Aeronautics and Space Administration (NASA) Earth Venture Suborbital 2 (EVS-2) mission, and its goal is to improve atmospheric inversion estimates of CO_2 and CH_4 through extensive airborne measurements over the eastern United Stated during multiple seasons (Davis et al., 2018a). Through four campaign seasons from Summer 2016 to Spring 2018 with two research aircraft (C130 and B200), the ACT project has collected an extensive dataset of highly resolved CO_2 measurements in both BL and FT. The duration of the ACT campaign seasons is given in Table 9. To use ACT airborne CO_2 measurements for model evaluation, we conducted a MPAS-A simulation lasts from January 1 2016 to May 31 2018. The first 6 months is for the model spin-up. The simulation uses the domain and configurations as described in Section. 3.1, and model outputs are saved at 1-hour intervals.

First we compare MPAS-A simulated horizontal wind fields during the ACT campaign seasons using the same procedure described in Section 3.3.1. Table 10 lists the statistics of horizontal wind fields evaluation at the four ACT campaign seasons. The table indicates the same pattern as in 2014 (Table 2): mean RMSE vector wind increases with altitude and mean difference of wind direction decreases with altitude. The magnitude of the statistics of the four ACT campaign seasons are comparable to that of 2014 (Table 2).

Next we use the ACT airborne measurements to evaluate MPAS-A CO_2 simulation regarding its overall accuracy and its performance measured by three model evaluation metrics proposed by Pal et al. (2020). To provide an objective reference, we also compare MPAS-A performance with two established CO_2 model systems: WRF-Chem (Skamarock et al., 2008) and CT2019 (Jacobson et al., 2020) using the same set of airborne measurements. WRF-Chem is an online CTM based on the regional model WRF (Grell et al., 2011; Skamarock et al., 2008). WRF-Chem simulations have been carried out at 27 km horizontal grid (Fig. S2) over North America as a part of the ACT project (Feng et al., 2020). The WRF-Chem simulations use ERA5 reanalysis (Hersbach et al., 2020) for meteorological initial and lateral boundary conditions, CarbonTracker (Jacobson et al., 2020) posterior mole fraction for CO_2 initial and boundary conditions, and CarbonTracker posterior fluxes for surface CO_2 fluxes. The WRF-Chem simulations use meteorological nudging and 120-hour meteorological re-initialization to keep meteorological fields close to the analysis.

CarbonTracker (Jacobson et al., 2020) is an operational carbon data-assimilation system which uses Transport Model 5 (TM5) (Krol et al., 2005) for atmospheric transport. TM5 is an offline global CTM which includes CO_2 advection, deep and shallow convection, and vertical diffusion in both PBL and free troposphere (Krol et al., 2005). In producing CT2019 CO_2 mole fraction (Jacobson et al., 2020), TM5 simulation ran over a $3^\circ \times 2^\circ$ global domain and an nested $1^\circ \times 1^\circ$ North America

domain driven by ERA-interim reanalysis (Dee et al., 2011).

We use the ACT 5-second averaged CO_2 measurement dataset (Davis et al., 2018b), which has a horizontal resolution approximately 500 m given the average aircraft velocity. MPAS simulated CO_2 fields are interpolated in time and space to match each 5-second airborne data points. WRF-Chem simulated CO_2 fields are also interpolated to match the ACT 5-second data point using the same approach as MPAS-A. CarbonTrack CO_2 used for the evaluation is obtained from CarbonTrack ObsPack (Masarie et al., 2014), which is the CT2019 posterior mole fraction interpolated to the ACT 5-second data points.

For each ACT flight day, CO_2 measurements from the two aircraft are combined if both are available, and their corresponding modeled CO_2 values from MPAS-A, WRF-Chem, and CT2019 are combined in the same way. With the four seasons combined, there are a total of 97 flight days (Pal and Davis, 2020), each one presented by an observation-model dataset consisted of observed CO_2, modeled CO_2 from the three models, along with the time, latitude, longitude, and altitude of each observation data point. Using the ACT maneuver flag dataset Pal et al. (2020), we further divide each flight day's data into two groups: one for BL and another for the free troposphere (FT). For each ACT campaign season, all the BL data-model pairs are combined for each of the three models for model comparison. Figure 8 shows the Taylor diagram of the model comparison in BL for the four campaign seasons. N in the title of each figure is the number of model-data pairs used for plotting the diagram. Similarly the model comparison in FT is summarized in the Taylor diagrams of Fig. 9. A comparison of Figs. 8 and 9 show that all three models have higher accuracy (lower RMSE) in FT than BL, which could be attributed to the larger error in the weather forecast in BL than FT associated with the accuracy of PBL height in the model simulation. Figure 8 shows that in BL, MPAS-A has higher RMSE and higher standard deviation than CT2019. MPAS-A has more accurate estimation of the observations' standard deviation than CT2019 in all but summer 2016. Compared with WRF-Chem, MPAS-A has lower RMSE and more accurate estimation of the observations' standard deviation. Figure 9 shows that in FT, MPAS-A has higher RMSE than CT2019 in all four campaign seasons and but it has more accurate estimation of the observations' standard deviation than CT2019 in all but summer 2016 season. Compared to WRF-Chem, MPAS-A has lower RMSE and more accurate estimation of observations' standard deviation in all but summer 2016.

3.4.1 Model representation of CO_2 difference between warm and cold sectors

Through analyzing the ACT Summer 2016 campaign data, Pal et al. (2020) identified three consistent features in CO_2 mole fraction and proposed to use these features as transport model assessment metrics. The three features are the differences between the warm and cold sectors, the difference between the boundary layer and free troposphere, and the CO_2 enhancement bands in the vicinity of frontal boundaries. Here and in the next two sections, we evaluate how MPAS-A simulated CO_2 represents the three features.

Using the ACT maneuver flag dataset (Pal et al., 2020), we identified flights that crossed a weather front and their associated warm and cold sectors. The CO_2 mole fraction statistics for the warm and cold sectors are calculated from the aircraft measurements and the modeled CO_2 by MPAS-A, WRF-Chem, and CT2019, respectively. The results are shown in Fig. 10, which summarizes the statistics of CO_2 mole fraction differences between the warm and cold sectors measured by 15 front-crossing flights: 10 from the summer 2016 season and 5 from the winter 2017 season. The figure confirms that the warm sector has higher average CO_2 mole fraction in the boundary layer than the cold sector during summer 2016 as reported by Pal et al. (2020). The figure also shows that the average CO_2 mole fraction in the warm sectors are lower than than the colder sectors in winter 2017, opposite to the summer 2016.

Table 11 lists the mean CO_2 of the warm sector, cold sectors, and their difference as calculated from the ACT measurements, MPAS-A, WRF-Chem, and CT2019. The table shows that the MPAS-A simulations are similar to WRF-Chem, and both tend to have larger CO_2 differences between the warm and cold sectors than CT2019. For instance, the 2016-08-08 case where the observed mean CO_2 difference between warm and cold sector is 26.9 ppm, MPAS-A and WRF simulations resulted in 36.9 ppm and 21.2 ppm respectively, while CT2019 resulted in a 15.3 ppm difference. The above evaluation indicates that MPAS-A CO_2 model is capable of well representing the observed CO_2 difference between the warm and cold sectors, and its accuracy in this respect is comparable to WRF-Chem and CT2019.

3.4.2 Model representation of CO_2 vertical difference

The second feature identified by Pal et al. (2020) is the vertical difference of CO_2 mole fraction between BL and FT. During ACT campaign season, two research aircraft (B200 and C130) took many vertical profile measurements during take off, landing, spiral up and down, and inline ascend and descend maneuvers (Pal, 2019). These profile observations characterize the vertical variation of the atmospheric CO_2 mole fraction. From the vertical profile measurements taken during the summer 2016 season, Pal et al. (2020) calculated the mean CO_2 mole fraction in BL and FT, denoted as $[CO_2]_{BL}$ and $[CO_2]_{FT}$ respectively. They further defined BL-to-FT CO_2 difference as $\Delta[CO_2] = [CO_2]_{BL} - [CO_2]_{FT}$. They found that $\Delta[CO_2]$ tend to be positive in the warm sector and negative in the cold sector. In this section, we evaluate how well MPAS-A represents the BL-to-FT CO_2 difference and compare its performance with WRF-Chem and CT2019.

Using the ACT maneuver flag dataset (Pal et al., 2020), we identified all vertical profiles taken during the four campaign seasons, from which we selected profiles that meet two criteria: (1) a vertical profile must include at least 20 5-second measurements in the boundary layer and 20 measurements in the free troposphere; and (2) a vertical profile must extend at least 2 km in the vertical direction. These two criteria are used to ensure that the resulting $[CO_2]_{BL}$ and $[CO_2]_{FT}$ are statistically representative. A total of 199 qualified vertical profiles are identified from the four campaign seasons, including 72 from the summer 2016 season, 27 from winter 2017, 40 from fall 2017, and 60 from spring 2018. For each of the vertical profiles, $\Delta[CO_2]$ is calculated for the aircraft CO_2 measurements, and the simulated CO_2 by MPAS-A, WRF-Chem, and CT2019. We compare

$\Delta[CO_2]$ from the models with that from the observations to assess how each model represents the observed BL-to-FT CO_2 difference. Figure 11 shows the comparisons grouped by the campaign seasons. The figure indicates a clear distinction in $\Delta[CO_2]$ between the summer 2016 and the other three seasons: There are a substantial number of both positive and negative $\Delta[CO_2]$ in the summer 2016 season, but the vast majority of cases in the rest of the three campaign seasons have positive $\Delta[CO_2]$. The positive BL-to-FT CO_2 differences from the winter 2017 season measurements could be at least partially attributable to the lack of CO_2 draw-down during the non-growing season. In comparison, the fall 2017 and spring 2018 seasons have more mixed results probably because of their partial overlap with the growing season. For the summer 2016 season, vertical profiles with negative $\Delta[CO_2]$ (lower mean CO_2 in BL than FT) suggest photosynthesis during the growing season, but those with positive $\Delta[CO_2]$ values are probably caused by the interaction between photosynthesis and frontal passage (Pal et al., 2020).

To compare the three models' accuracy in representing the BL-TO-FT CO_2 difference, we calculated the mean absolute error (MAE) for each model at each season, where $\mathrm{AE} = |\Delta[CO_2]_{\mathrm{model}} - \Delta[CO_2]_{\mathrm{obs}}|$ (the absolute difference in $\Delta[CO_2]$ between a model and the ACT observations).

$$\mathrm{MAE} = \frac{1}{N}\sum_{i=1}^{N}\mathrm{AE}_i \tag{21}$$

Table 12 summarize the MAE of the three models for each season. The p values of paired t tests of AE between MPAS-A and the other two models are also listed in the table to provide the significance level of the model comparisons. Using $p = 0.1$ as the cut-off value the table shows that MPAS-A has smaller MAE than CT2019 in fall 2017 and a larger MAE in summer 2016. The differences between the two models in the other two seasons are not significant. Compared to WRF-Chem, MPAS-A has smaller MAEs in winter 2017 and spring 2018 while the differences in the other two seasons are not significant. In summary, the above model evaluation and comparison demonstrate that MPAS-A CO_2 transport model is capable of representing the aircraft observed CO_2 difference between BL and FT at least as accurately as WRF-Chem and CT2019.

3.4.3 Model representation of CO_2 enhancement at frontal boundaries

The third feature identified by Pal et al. (2020) in the summer 2016 aircraft measurements is the bands of enhanced CO_2 close to frontal boundaries in BL. They found these CO_2 enhancement bands are typically about 100 km wide and speculated that it would require a 20-km horizontal resolution model to effectively represent the feature. In this section, we identify the frontal boundary CO_2 enhancements in the four campaign seasons and examine how well they are represented by MPAS-A.

Using the same approach as Pal et al. (2020), a total of 48 front-crossing constant-altitude flight segments are identified from the four seasons (15 from Summer 2016, 5 from Winter 2017, 17 from Fall 2017, and 11 from Fall 2018). To evaluate how well MPAS-A represents the frontal boundary CO_2 enhancements and compare its performance with WRF-Chem and CT2019, CO_2 mole fraction measured by the aircraft and simulated by the three models are plotted together for each of the identified

front-crossing constant-altitude flight segment. Figure 12 includes 8 of the front-crossing flight segments and the full set is included in Fig. S3 of supplement. For each flight segment in Fig. 12, the pair of vertical dashed lines mark CO_2 enhancement observed by the aircraft along a frontal boundary. The warm and cold sectors associated with the frontal boundary in each flight are labeled as warm and cold respectively. The figure indicates that frontal boundary CO_2 enhancements can be identified in most of the flight segments but not all cases. For instance, there is not clearly identifiable CO_2 enhancement in the B200 flights on 2018-04-23 (Fig. S3).

Figure 12 shows that MPAS-A has a varying degree of success in simulating the frontal boundary CO_2 enhancements: it represents both the timing and the magnitude of the enhancements very well in some cases (2016-08-04 and 2017-10-18 by B200), but results in substantial errors in either the timing (2016-07-25 B200) or the magnitude (2017-03-10 C130) in other cases. The figure also shows that the MPAS-A simulated CO_2 is more similar to WRF-Chem than CT2019: CT2019 tends to substantially underestimate the magnitude of CO_2 enhancement while MPAS-A and WRF-Chem tend to overestimate.

Figure 13 shows the MPAS-A simulated equivalent potential temperature (θ_e) and CO_2 mole fraction at 18:00 UTC August 4, 2016. The sharp boundary in θ_e indicates a surface cold front extending from southern Colorado northeastward to Wisconsin. Abrupt horizontal wind direction changes shown in Fig. S4 of the supplement also indicate the cold front and its southeastward movement. Meteorological measurements taken during the flight (not shown) also confirm the cold front passage. The B200 research aircraft crossed the cold front from southeast to northwest at about 400-500 meters above the ground between 17:15 UTC and 19:15 UTC, and its flight track and timing are marked on Fig. 13. The aircraft measurements show an approximately 20 ppm enhancement along the front boundary, which can be clearly identified in the MPAS-A simulated CO_2 mole fraction (lower panel of Fig. 13).

Figure 14 compares the three models in their representation of the frontal boundary CO_2 variation. The figure shows that except for summer 2016, MPAS-A has similar level of RMSE as CT2019 and it has more accurate estimation of the observations' standard deviation. As horizontal resolution impacts a model's ability to represent small scale spatial variability (Agusti-Panareda et al., 2019), the coarser resolution of CT2019 ($1^\circ \times 1^\circ$ over the North America) is likely the primary cause of its underestimation of the frontal boundary CO_2 variability. MPAS-A has lower RMSE than WRF-Chem in winter 2017 and spring 2018, and similar RMSE as WRF-Chem in the other two seasons. In all but summer 2016, MPAS-A has more an accurate estimation of the observations' standard deviation than WRF-Chem.

4 Summary

We implemented the CO_2 atmospheric transport processes, including advection, vertical mixing, and convective transport, in the global variable-resolution model MPAS-A. After the model development details are presented, simulation experiments designed for model evaluation are described. Two sets of simulations over a 60-15 km variable-resolution global domain are

conducted for model accuracy evaluation using an extensive aircraft measurements over the eastern United States and near-surface hourly measurements from surface and tower stations distributed across the globe. Meteorological initial conditions for these simulations are from the ERA-interim analysis (Dee et al., 2011), and CO_2 initial conditions and fluxes are from CT2019 posterior mole fraction and fluxes products (Jacobson et al., 2020). To keep model meteorological fields close to the analysis, meteorology re-initialization are applied at 24-hour interval throughout the simulation periods. Global CO_2 mass conservation property is assessed by a one-year continuous simulation without meteorology re-initialization and fluxes, and the results show that MPAS-A is capable of maintaining total dry air mass conservation to the limit of machine precision. During the one-year simulation period, the total CO_2 mass change is about 10^{-5} of its initial value. The larger variation of CO_2 mass than the dry air is due to the complex and strong spatial gradient caused by the surface CO_2 fluxes. Another one-year simulation with meteorology re-initialization indicates that changes in dry air density during the re-initialization causes changes in global total CO_2 mass, and a scaling method applied after each re-initialization is able to reduce the change from $\sim 10^{-4}$ to $\sim 10^{-6}$ of the global CO_2 mass.

The accuracy of MPAS-A CO_2 transport is evaluated first at the global scale and then at the regional scale. At the global scale, MPAS-A simulation is evaluated using CT2019, near-surface hourly CO_2 measurements from 50 stations and XCO_2 measurements from 18 TCCON stations. The resulting statistics are compared with the ECWMF IFS 9km and 80 km resolution simulations over the same period conducted by Agusti-Panareda et al. (2019). The comparison indicates that RMSE of the MPAS-A simulation is similar to the 80 km IFS simulation, but larger than the 9 km IFS simulation.

At the regional scale, A MPAS-A simulation extending from January 1 2016 to June 1 2018 is evaluated using the extensive high-resolution aircraft measurements from four ACT campaign seasons. Compared with a 27 km resolution WRF-Chem simulation and CT2019 posterior CO_2 mole fraction, MPAS-A simulated CO_2 achieves a comparable level of accuracy (as measured by RMSE). Further evaluation using three metrics proposed by Pal et al. (2020) shows that MPAS-A simulation is capable of representing the observed CO_2 features as accurately as the WRF-Chem simulation and CT2019.

The model evaluations using the airborne and near-surface measurements, indicates that the newly developed MPAS-A CO_2 transport model is capable of achieving a comparable level of accuracy with the more established CO_2 modeling systems, including the regional model system WRF-Chem, the operational assimilation system CarbonTracker, and the lower resolution (80 km) simulation of ECWMF IFS global CO_2 modeling system. Although further improvements are expected, the MPAS-A CO_2 transport model has the potential to contribute to improving our knowledge of atmospheric CO_2 transport and fluxes.

Code and data availability

Source code for MPAS-A CO_2 transport model v6.3 can be retrieved at https://doi.org/10.5281/zenodo.3976320. Source code for WRF-Chem v3.6 used in the manuscript can be obtained from NCAR website at

http://www2.mmm.ucar.edu/wrf/users/download/get_source.html. Source code for IFS is only available subject to a licence agreement with ECMWF. ECMWF member-state weather services and their approved partners will get access granted. The IFS source code without modules for assimilation and chemistry can be obtained for educational and academic purposes as part of the openIFS release (https:// software.ecmwf.int/wiki/display/OIFS/OpenIFS+Home). ACT-America in-situ Airborne CO_2 measurement data can be obtained at https://doi.org/10.3334/ORNLDAAC/1593. Surface and tower based CO_2 measurement data from ObsPack GLOBALVIEWplus v6.0 can be obtained from NOAA website https://esrl.noaa.gov/gmd/ccgg/obspack/data.php. CarbonTrack CO_2 flux and posterior mixing ratio data can be obtained from NOAA website https://www.esrl.noaa.gov/gmd/ccgg/carbontracker/download.php.

Author contributions

TZ implemented the CO_2 transport processes in MPAS-A v6.3. SF conducted the WRF-Chem 27km simulations. TZ, SF, KD, SP designed model evaluation using ACT-America aircraft measurements. TZ and JM designed the model evaluation using continuous in-situ tower measurements. TZ, SF, KD, SP analyzed the model representation of distinct CO_2 spatial features observed by the aircraft measurements. All authors contributed to writing and commenting on the paper.

Acknowledgment

We thank the MPAS-A development team for making their code available for the public; we thank NOAA CarbonTracker team for providing the CT2019 flux and mole fraction data; we thank ECWMF for the ERA-interim analysis data; we thank ObsPack data providers for the in-situ continuous CO_2 measurement data. TZ was supported by a Central Michigan University Research Incentive Fund. FS and KD were supported by the Atmospheric Carbon and Transport-America (ACT) Earth Venture Suborbital 2 project funded by NASA's Earth Science Division (Grant NNX15AG76G to Penn State), SP was supported by NASA Grant Number 80NSSC19K0730 and a Texas Tech University start up research grant. This work was supported in part through computational resources and services provided by the Institute for Cyber-Enabled Research at Michigan State University.

References

Agusti-Panareda, A., Massart, S., Chevallier, F., Boussetta, S., Balsamo, G., Beljaars, A., Ciais, P., Deutscher, N. M., Engelen, R., Jones, L., Kivi, R., Paris, J.-D., Peuch, V.-H., Sherlock, V., Vermeulen, A. T., Wennberg, P. O., and Wunch, D.: Forecasting global atmospheric CO_2, Atmospheric Chemistry and Physics, 14, 11 959–11 983, doi:10.5194/acp-14-11959-2014, https://www.atmos-chem-phys.net/14/11959/2014/, 2014.

Agusti-Panareda, A., Diamantakis, M., Bayona, V., Klappenbach, F., and Butz, A.: Improving the inter-hemispheric gradient of total column atmospheric CO_2 and CH_4 in simulations with the ECMWF semi-Lagrangian atmospheric global model, Geoscientific Model Development, 10, 1–18, doi:10.5194/gmd-10-1-2017, https://gmd.copernicus.org/articles/10/1/2017/, 2017.

Agusti-Panareda, A., Diamantakis, M., Massart, S., Chevallier, F., Munoz-Sabater, J., Barre, J., Curcoll, R., Engelen, R., Langerock, B., Law, R. M., Loh, Z., Anton Morgui, J., Parrington, M., Pench, V.-H., Ramonet, M., Roehl, C., Vermeulen, A. T., Warneke, T., and Wunch, D.: Modelling CO2 weather - why horizontal resolution matters, Atmospheric Chemistry and Physics, 19, 7347–7376, doi:10.5194/acp-19-7347-2019, 2019.

Andrews, A. E., Kofler, J. D., Trudeau, M. E., Williams, J. C., Neff, D. H., Masarie, K. A., Chao, D. Y., Kitzis, D. R., Novelli, P. C., Zhao, C. L., Dlugokencky, E. J., Lang, P. M., Crotwell, M. J., Fischer, M. L., Parker, M. J., Lee, J. T., Baumann, D. D., Desai, A. R., Stanier, C. O., De Wekker, S. F. J., Wolfe, D. E., Munger, J. W., and Tans, P. P.: CO_2, CO, and CH_4 measurements from tall towers in the NOAA Earth System Research Laboratory's Global Greenhouse Gas Reference Network: instrumentation, uncertainty analysis, and recommendations for future high-accuracy greenhouse gas monitoring efforts, Atmospheric Measurement Techniques, 7, 647–687, doi:10.5194/amt-7-647-2014, https://www.atmos-meas-tech.net/7/647/2014/, 2014.

Baker, D. F., Doney, S. C., and Schimel, D. S.: Variational data assimilation for atmospheric CO2, Tellus B, 58, 359–365, 2006.

Blumenstock, T., Hase, F., Schneider, M., García, O. E., and Sepúlveda, E.: TCCON data from Izana (ES), Release GGG2014.R1, doi:10.14291/TCCON.GGG2014.IZANA01.R1, https://data.caltech.edu/records/302, 2017.

Borge, R., Alexandrov, V., del Vas, J. J., Lumbreras, J., and Rodriguez, E.: A comprehensive sensitivity analysis of the WRF model for air quality applications over the Iberian Peninsula, Atmospheric Environment, 42, 8560–8574, doi:10.1016/j.atmosenv.2008.08.032, 2008.

Brunke, E., Labuschagne, C., Parker, B., Scheel, H., and Whittlestone, S.: Baseline air mass selection at Cape Point, South Africa: application of Rn-222 and other filter criteria to CO2, Atmospheric Environment, 38, 5693–5702, doi:10.1016/j.atmosenv.2004.04.024, 2004.

Chen, F. and Dudhia, J.: Coupling an advanced land surface-hydrology model with the Penn State-NCAR MM5 modeling system. Part I: Model implementation and sensitivity, Monthly Weather Review, 129, 569–585, doi:10.1175/1520-0493(2001)129<0569:CAALSH>2.0.CO;2, 2001.

Conway, T. J. and Thoning, K. W.: Short-term variations of atmospheric carbon dioxide at the South Pole, Anarctic Journal, pp. 236–238, 1990.

Davies, T.: Lateral boundary conditions for limited area models, Quarterly Journal of the Royal Meteorological Society, 140, 185–196, doi:10.1002/qj.2127, 2014.

Davis, K., Baier, B., Z., B., Bowman, K., Boyer, A., and Browell, E.: Atmospheric Carbon and Transport (ACT)- America: A multi-year airborne mission to study fluxes and transport of CO2 and CH4 across the eastern United States, american Geophysical Union Fall Meeting, 2018a.

Davis, K., Obland, M., Lin, B., Lauvaux, T., O'Dell, C., Meadows, B., Browell, E., DiGangi, J., Sweeney, C., McGill, M., Barrick, J., Nehrir, A., Yang, M., Bennett, J., Baier, B., Roiger, A., Pal, S., Gerken, T., Fried, A., Feng, S., Shrestha, R., Shook, M., Chen, G.,

Campbell, L., Barkley, Z., and Pauly, R.: ACT-America: L3 Merged In Situ Atmospheric Trace Gases and Flask Data, Eastern USA, doi:10.3334/ORNLDAAC/1593, https://daac.ornl.gov/cgi-bin/dsviewer.pl?ds_id=1593, 2018b.

De Mazière, M., Sha, M. K., Desmet, F., Hermans, C., Scolas, F., Kumps, N., Metzger, J.-M., Duflot, V., and Cammas, J.-P.: TCCON data from Réunion Island (RE), Release GGG2014.R0, doi:10.14291/TCCON.GGG2014.REUNION01.R0/1149288, https://data.caltech.edu/records/286, 2014.

Dee, D. P., Uppala, S. M., Simmons, A. J., Berrisford, P., Poli, P., Kobayashi, S., Andrae, U., Balmaseda, M. A., Balsamo, G., Bauer, P., Bechtold, P., Beljaars, A. C. M., van de Berg, L., Bidlot, J., Bormann, N., Delsol, C., Dragani, R., Fuentes, M., Geer, A. J., Haimberger, L., Healy, S. B., Hersbach, H., Holm, E. V., Isaksen, L., Kallberg, P., Koehler, M., Matricardi, M., McNally, A. P., Monge-Sanz, B. M., Morcrette, J. J., Park, B. K., Peubey, C., de Rosnay, P., Tavolato, C., Thepaut, J. N., and Vitart, F.: The ERA-Interim reanalysis: configuration and performance of the data assimilation system, Quarterly Journal of the Royal Meteorological Society,, 137, 553–597, doi:10.1002/qj.828, 2011.

Deutscher, N. M., Notholt, J., Messerschmidt, J., Weinzierl, C., Warneke, T., Petri, C., and Grupe, P.: TCCON data from Bialystok (PL), Release GGG2014.R1, doi:10.14291/TCCON.GGG2014.BIALYSTOK01.R1/1183984, https://data.caltech.edu/records/267, 2015.

Diamantakis, M. and Flemming, J.: Global mass fixer algorithms for conservative tracer transport in the ECMWF model, Geoscientific Model Development, 7, 965–979, doi:10.5194/gmd-7-965-2014, https://gmd.copernicus.org/articles/7/965/2014/, 2014.

Diaz-Isaac, L. I., Lauvaux, T., and Davis, K. J.: Impact of physical parameterizations and initial conditions on simulated atmospheric transport and CO2 mole fractions in the US Midwest, Atmospheric Chemistry and Physics, 18, 14 813–14 835, doi:10.5194/acp-18-14813-2018, 2018.

Diaz-Isaac, L. I., Lauvaux, T., Bocquet, M., and Davis, K. J.: Calibration of a multi-physics ensemble for estimating the uncertainty of a greenhouse gas atmospheric transport model, Atmospheric Chemistry and Physics, 19, 5695–5718, doi:10.5194/acp-19-5695-2019, 2019.

Feist, D. G., Arnold, S. G., John, N., and Geibel, M. C.: TCCON data from Ascension Island, Saint Helena, Ascension and Tristan da Cunha, Release GGG2014R0, TCCON data archive, hosted by the Carbon Dioxide Information Analysis Center, Oak Ridge National Laboratory, Oak Ridge, Tennessee, USA, doi:doi:10.14291/tccon.ggg2014.ascension01.R0/1149285, 2014.

Feng, S., Lauvaux, T., Barkley, Z. R, D. k. J., Butler, M. B., Deng, A., Gaudet, B., and D., S.: Full WRF-Chem output in support of the NASA Atmospheric Carbon and Transport (ACT)-America project (7/1/2016 – 7/31/2019). The Pennsylvania State University Data Commons, University Park, Pennsylvania, USA, doi:10.26208/49kd-b637, https://doi.org/10.26208/49kd-b637, 2020.

Feng, S., Lauvaux, T., Newman, S., Rao, P., Ahmadov, R., Deng, A., Diaz-Isaac, L. I., Duren, R. M., Fischer, M. L., Gerbig, C., Gurney, K. R., Huang, J., Jeong, S., Li, Z., Miller, C. E., O'Keeffe, D., Patarasuk, R., Sander, S. P., Song, Y., Wong, K. W., and Yung, Y. L.: Los Angeles megacity: a high-resolution land-atmosphere modelling system for urban CO_2 emissions, Atmospheric Chemistry and Physics, 16, 9019–9045, doi:10.5194/acp-16-9019-2016, 2016.

Feng, S., Lauvaux, T., Davis, K. J., Keller, K., Zhou, Y., Williams, C., Schuh, A. E., Liu, J., and Baker, I.: Seasonal Characteristics of Model Uncertainties From Biogenic Fluxes, Transport, and Large-Scale Boundary Inflow in Atmospheric CO2 Simulations Over North America, Journal of Geophysical Research-Atmospheres, 124, 14 325–14 346, doi:10.1029/2019JD031165, 2019.

Francey, R. J., Steele, L. P., Spencer, D. A., Langenfelds, R. L., Law, R. M., Krummel, P. B., Fraser, P. J., Etheridge, D. M., Derek, N., Coram, S. A., Cooper, L. N., Allison, C. E., Porter, L., and Baly, S.: The CSIRO (Australia) measurement of greenhouse gases in the global atmosphere, report of the 11th WMO/IAEA Meeting of Experts on Carbon Dioxide Concentration and Related Tracer Measurement Techniques, Tokyo, Japan, September 2001, edited by: Toru, S. and Kazuto, S., World Meteorological Organization Global Atmosphere Watch, 2003.

Fritsch, J. M. and Chappell, C. F.: Numerical prediction of convectively driven mesoscale pressure systems. Part I: convective parameterization, Journal of the Atmospheric Sciences, 37, 1722–1733, doi:10.1175/1520-0469(1980)037<1722:NPOCDM>2.0.CO;2, 1980.

Gaudry, A., Monfray, P., Polian, G., Bonsang, G., Ardouin, B., Jegou, A., and Lambert, G.: Nonseasonnal variations of atmospheric CO2 concentrations at Amsterdam Island, Tellus Series B-Chemical and Physical Meteorology, 43, 136–143, doi:10.1034/j.1600-0889.1991.00008.x, 1991.

Gerbig, C., Körner, S., and Lin, J. C.: Vertical mixing in atmospheric tracer transport models: error characterization and propagation, Atmospheric Chemistry and Physics, 8, 591–602, doi:10.5194/acp-8-591-2008, 2008.

Gerbig, C., Dolman, A. J., and Heimann, M.: On observational and modelling strategies targeted at regional carbon exchange over continents, Biogeosciences, 6, 1949–1959, doi:10.5194/bg-6-1949-2009, 2009.

Gockede, M., Turner, D. P., Michalak, A. M., Vickers, D., and Law, B. E.: Sensitivity of a subregional scale atmospheric inverse CO2 modeling framework to boundary conditions, Journal of Geophysical Research, 115, doi:10.1029/2010JD014443, 2010.

Golaz, J.-C., Caldwell, P. M., Van Roekel, L. P., Petersen, M. R., Tang, Q., Wolfe, J. D., and et al.: The DOE E3SM Coupled Model Version 1: Overview and Evaluation at Standard Resolution, Journal of Advances in Modeling Earth Systems, 11, 2089–2129, doi:10.1029/2018MS001603, 2019.

Gomez-Pelaez, A. J. and Ramos, R.: Improvements in the Carbon Dioxide and Methane Continuous Measurement Programs at Izana Global GAW Station (Spain) during 2007–2009, in: GAW report (No. 194) of the 15th WMO/IAEA Meeting of Experts on Carbon Dioxide, Other Greenhouse Gases, and Related Tracer Measurement Techniques (Jena, Germany; 7–10 September 2009), edited by: Brand, W. A., World Meteorological Organization (TD No. 1553), 2005.

Grell, G., Freitas, S. R., Stuefer, M., and Fast, J.: Inclusion of biomass burning in WRF-Chem: impact of wildfires on weather forecasts, Atmospheric Chemistry and Physics, 11, 5289–5303, doi:10.5194/acp-11-5289-2011, 2011.

Griffith, D. W., Deutscher, N. M., Velazco, V. A., Wennberg, P. O., Yavin, Y., Keppel-Aleks, G., Washenfelder, R. A., Toon, G. C., Blavier, J.-F., Paton-Walsh, C., Jones, N. B., Kettlewell, G. C., Connor, B. J., Macatangay, R. C., Roehl, C., Ryczek, M., Glowacki, J., Culgan, T., and Bryant, G. W.: TCCON data from Darwin (AU), Release GGG2014.R0, doi:10.14291/TCCON.GGG2014.DARWIN01.R0/1149290, https://data.caltech.edu/records/269, 2014a.

Griffith, D. W., Velazco, V. A., Deutscher, N. M., Paton-Walsh, C., Jones, N. B., Wilson, S. R., Macatangay, R. C., Kettlewell, G. C., Buchholz, R. R., and Riggenbach, M. O.: TCCON data from Wollongong (AU), Release GGG2014.R0, doi:10.14291/TCCON.GGG2014.WOLLONGONG01.R0/1149291, https://data.caltech.edu/records/291, 2014b.

Halter, B., Harris, J., and Conway, T.: Component signals in the record of atmospheric carbon dioxide concentration at American Samoa, Journal of Geophysical Research-Atmospheres, 93, 15 914–15 918, doi:10.1029/JD093iD12p15914, 1988.

Hase, F., Blumenstock, T., Dohe, S., Groß, J., and Kiel, M.: TCCON data from Karlsruhe (DE), Release GGG2014.R1, doi:10.14291/TCCON.GGG2014.KARLSRUHE01.R1/1182416, https://data.caltech.edu/records/278, 2015.

Haszpra, L., Barcza, Z., Bakwin, P., Berger, B., Davis, K., and Weidinger, T.: Measuring system for the long-term monitoring of biosphere/atmosphere exchange of carbon dioxide, Journal of Geophysical Research-Atmospheres, 106, 3057–3069, doi:10.1029/2000JD900600, 2001.

Hatakka, J., Aalto, T., Aaltonen, V., Aurela, M., Hakola, H., Komppula, M., Laurila, T., Lihavainen, H., Paatero, J., Salminen, K., and Viisanen, Y.: Overview of the atmospheric research activities and results at Pallas GAW station, Boreal Environment Research, 8, 365–383, 2003.

Hersbach, H., Bell, B., Berrisford, P., Hirahara, S., Horanyi, A., Munoz-Sabater, J., Nicolas, J., Peubey, C., Radu, R., Schepers, D., Simmons, A., Soci, C., Abdalla, S., Abellan, X., Balsamo, G., Bechtold, P., Biavati, G., Bidlot, J., Bonavita, M., De Chiara, G., Dahlgren, P., Dee, D., Diamantakis, M., Dragani, R., Flemming, J., Forbes, R., Fuentes, M., Geer, A., Haimberger, L., Healy, S., Hogan, R. J., Holm, E., Janiskova, M., Keeley, S., Laloyaux, P., Lopez, P., Lupu, C., Radnoti, G., de Rosnay, P., Rozum, I., Vamborg, F., Villaume, S., and Thepaut, J.-N.: The ERA5 global reanalysis, Quaterly Journal of the Royal Meteorological Society, 146, 1999–2049, doi:10.1002/qj.3803, 2020.

Hong, S., Dudhia, J., and Chen, S.: A revised approach to ice microphysical processes for the bulk parameterization of clouds and precipitation, Monthly Weather Review, 132, 103–120, doi:10.1175/1520-0493(2004)132<0103:ARATIM>2.0.CO;2, 2004.

Hong, S.-Y. and Lim, J.: Journal of the Korean Meteorological Society, 42, 29–151, 2006.

Hong, S.-Y., Noh, Y., and Dudhia, J.: A new vertical diffusion package with an explicit treatment of entrainment processes, Monthly Weather Review, 134, 2318–2341, doi:10.1175/MWR3199.1, 2006.

Hu, L., Andrews, A. E., Thoning, K. W., Sweeney, C., Miller, J. B., Michalak, A. M., Dlugokencky, E., Tans, P. P., Shiga, Y. P., Mountain, M., Nehrkorn, T., Montzka, S. A., McKain, K., Kofler, J., Trudeau, M., Michel, S. E., Biraud, S. C., Fischer, M. L., Worthy, D. E. J., Vaughn, B. H., White, J. W. C., Yadav, V., Basu, S., and van der Velde, I. R.: Enhanced North American carbon uptake associated with El Niño, Science Advances, 5, doi:10.1126/sciadv.aaw0076, 2019.

Hu, X.-M., Nielsen-Gammon, J. W., and Zhang, F.: Evaluation of Three Planetary Boundary Layer Schemes in the WRF Model, Journal of Applied Meteorology Climatol., 49, 1831–1844, 2010.

Iacono, M. J., Delamere, J. S., Mlawer, E. J., Shephard, M. W., Clough, S. A., and Collins, W. D.: Radiative forcing by long-lived greenhouse gases: Calculations with the AER radiative transfer models, Journal of Geophysical Research-Atmospheres, 113, doi:10.1029/2008JD009944, 2008.

Iraci, L. T., Podolske, J. R., Hillyard, P. W., Roehl, C., Wennberg, P. O., Blavier, J.-F., Landeros, J., Allen, N., Wunch, D., Zavaleta, J., Quigley, E., Osterman, G. B., Albertson, R., Dunwoody, K., and Boyden, H.: TCCON data from Edwards (US), Release GGG2014.R1, doi:10.14291/TCCON.GGG2014.EDWARDS01.R1/1255068, https://data.caltech.edu/records/270, 2016.

Jacobson, A. R., Fletcher, S. E. M., Gruber, N., Sarmiento, J. L., and Gloor, M.: A joint atmosphere-ocean inversion for surface fluxes of carbon dioxide: 1. Methods and global-scale fluxes, Global Biogeochemical Cycles, 21, doi:10.1029/2006GB002703, gB1019, 2007.

Jacobson, A. R., Schuldt, K. N., Miller, J. B., Oda, T., Tans, P., Arlyn Andrews, Mund, J., Ott, L., Collatz, G. J., Aalto, T., Afshar, S., Aikin, K., Aoki, S., Apadula, F., Baier, B., Bergamaschi, P., Beyersdorf, A., Biraud, S. C., Bollenbacher, A., Bowling, D., Brailsford, G., Abshire, J. B., Chen, G., Huilin Chen, Lukasz Chmura, Sites Climadat, Colomb, A., Conil, S., Cox, A., Cristofanelli, P., Cuevas, E., Curcoll, R., Sloop, C. D., Davis, K., Wekker, S. D., Delmotte, M., DiGangi, J. P., Dlugokencky, E., Ehleringer, J., Elkins, J. W., Emmenegger, L., Fischer, M. L., Forster, G., Frumau, A., Galkowski, M., Gatti, L. V., Gloor, E., Griffis, T., Hammer, S., Haszpra, L., Hatakka, J., Heliasz, M., Hensen, A., Hermanssen, O., Hintsa, E., Holst, J., Jaffe, D., Karion, A., Kawa, S. R., Keeling, R., Keronen, P., Kolari, P., Kominkova, K., Kort, E., Krummel, P., Kubistin, D., Labuschagne, C., Langenfelds, R., Laurent, O., Laurila, T., Lauvaux, T., Law, B., Lee, J., Lehner, I., Leuenberger, M., Levin, I., Levula, J., Lin, J., Lindauer, M., Loh, Z., Lopez, M., Myhre, C. L., Machida, T., Mammarella, I., Manca, G., Manning, A., Manning, A., Marek, M. V., Marklund, P., Martin, M. Y., Matsueda, H., McKain, K., Meijer, H., Meinhardt, F., Miles, N., Miller, C. E., Mölder, M., Montzka, S., Moore, F., Josep-Anton Morgui, Morimoto, S., Munger, B., Jaroslaw Necki, Newman, S., Nichol, S., Niwa, Y., O'Doherty, S., Mikaell Ottosson-Löfvenius, Paplawsky, B., Peischl, J., Peltola, O., Jean-Marc Pichon, Piper, S., Plass-Dölmer, C., Ramonet, M., Reyes-Sanchez, E., Richardson, S., Riris, H., Ryerson, T., Saito, K., Sargent, M., Sasakawa, M., Sawa, Y., Say, D., Scheeren, B., Schmidt, M., Schmidt, A., Schumacher, M., Shepson, P., Shook, M., Stanley, K., Steinbacher, M., Stephens, B., Sweeney, C., Thoning, K., Torn, M., Turnbull, J., Tørseth, K., Bulk, P. V. D., Laan-Luijkx, I. T. V. D., Dinther, D. V., Vermeulen, A.,

Viner, B., Vitkova, G., Walker, S., Weyrauch, D., Wofsy, S., Worthy, D., Dickon Young, and Miroslaw Zimnoch: CarbonTracker CT2019, doi:10.25925/39M3-6069, https://www.esrl.noaa.gov/gmd/ccgg/carbontracker/CT2019/, 2020.

Kain, J. S.: The Kain–Fritsch Convective Parameterization: An Update, Journal of Applied Meteorology, 43, 170–181, doi:10.1175/1520-0450(2004)043<0170:TKCPAU>2.0.CO;2, 2004.

Kain, J. S. and Fritsch, J. M.: A one-dimensional entraining detraining plume model and its application in convective parameterization, Journal of the Atmospheric Sciences, 47, 2784–2802, doi:10.1175/1520-0469(1990)047<2784:AODEPM>2.0.CO;2, 1990.

Kawakami, S., Ohyama, H., Arai, K., Okumura, H., Taura, C., Fukamachi, T., and Sakashita, M.: TCCON data from Saga (JP), Release GGG2014.R0, doi:10.14291/TCCON.GGG2014.SAGA01.R0/1149283, https://data.caltech.edu/records/288, 2014.

Kivi, R., Heikkinen, P., and Kyro: TCCON data from Sodankyla, Finland, Release GGG2014R0., TCCON data archive, hosted by the Carbon Dioxide Information Analysis Center, Oak Ridge National Laboratory, Oak Ridge, Tennessee, USA, doi:doi:10.14291/tccon.ggg2014.sodankyla01.R0/1149280, 2014.

Kretschmer, R., Gerbig, C., Karstens, U., and Koch, F. T.: Error characterization of CO2 vertical mixing in the atmospheric transport model WRF-VPRM, Atmospheric Chemistry and Physics, 12, 2441–2458, 2012.

Krol, M., Houweling, S., Bregman, B., van den Broek, M., Segers, A., van Velthoven, P., Peters, W., Dentener, F., and Bergamaschi, P.: The two-way nested global chemistry-transport zoom model TM5: algorithm and applications, Atmospheric Chemistry and Physics, 5, 417–432, doi:10.5194/acp-5-417-2005, 2005.

Lauvaux, T. and Davis, K. J.: Planetary boundary layer errors in mesoscale inversions of column-integrated CO_2 measurements, Journal of Geophysical Research-Atmospheres, 119, 490–508, doi:10.1002/2013JD020175, 2014.

Lauvaux, T., Schuh, A. E., Uliasz, M., Richardson, S., Miles, N., Andrews, A. E., Sweeney, C., Diaz, L. I., Martins, D., Shepson, P. B., and Davis, K. J.: Constraining the CO_2 budget of the corn belt: exploring uncertainties from the assumptions in a mesoscale inverse system, Atmospheric Chemistry and Physics, 12, 337–354, doi:10.5194/acp-12-337-2012, https://www.atmos-chem-phys.net/12/337/2012/, 2012.

Loh, Z. M., Law, R. M., Ziehn, T., van der Schoot M. V., Krummel, P. B., Steele, L. P., Etheridge, D. M., Spencer, D. A., Gregory, R. L., Langenfelds, R. L., Stavert, A. R., and Thornton, D. P.: The Australian Greenhouse Gas Observation Network: Current status and vision for the future. 10th International Carbon Dioxide Conference (ICDC10),21–25 August 2017,Interlaken, Switzerland, http://www.icdc10.unibe.ch/unibe/portal/fak_naturwis/micro_icdc10/content/e342182/e604227/e604229/files623284/Loh_Zoe.pdf, 2017.

Lopez, M., Schmidt, M., Ramonet, M., Bonne, J.-L., Colomb, A., Kazan, V., Laj, P., and Pichon, J.-M.: Three years of semicontinuous greenhouse gas measurements at the Puy de Dôme station (central France), Atmospheric Measurement Techniques, 8, 3941–3958, doi:10.5194/amt-8-3941-2015, 2015.

Louis, J. F.: A parametric model of vertical eddy flux in the atmosphere, Boundary Layer Meteorology, 17, 187–202, 1979.

Masarie, K. A., Peters, W., Jacobson, A. R., and Tans, P. P.: ObsPack: a framework for the preparation, delivery, and attribution of atmospheric greenhouse gas measurements, Earth System Science Data, 6, 375–384, doi:10.5194/essd-6-375-2014, 2014.

Morgui, J. A., Agueda, A., Batet, O.and Curcoll, R., Ealo, M., G. C., Occhipinti, P., Sanchez-Garcia, L., Arias, R., and Rodo, X.: ClimaDat: A long-term network to study at different scales climatic processes and interactions between climatic compartments, Geophys. Res. Abstr., EGU13-10265, EGU General Assembly 2013, Vienna, Austria, 2013, 2013.

Morino, I., Matsuzaki, T., and Horikawa, M.: TCCON data from Tsukuba (JP), 125HR, Release GGG2014.R1, doi:10.14291/TCCON.GGG2014.TSUKUBA02.R1/1241486, https://data.caltech.edu/records/290, 2016a.

Morino, I., Yokozeki, N., Matsuzaki, T., and Horikawa, M.: TCCON data from Rikubetsu (JP), Release GGG2014.R1, doi:10.14291/TCCON.GGG2014.RIKUBETSU01.R1/1242265, https://data.caltech.edu/records/287, 2016b.

Necki, J., Schmidt, M., Rozanski, K., Zimnoch, M., Korus, A., Lasa, J., Graul, R., and Levin, I.: Six-year record of atmospheric carbon dioxide and methane at a high-altitude mountain site in Poland, Tellus Series B-Chemical and Physical Meteorology, 55, 94–104, doi:10.1034/j.1600-0889.2003.01446.x, 2003.

Noh, Y., Cheon, W., Hong, S., and Raasch, S.: Improvement of the K-profile model for the planetary boundary layer based on large eddy simulation data, Boundary Layer Meteorology, 107, 401–427, doi:10.1023/A:1022146015946, 2003.

Notholt, J., Petri, C., Warneke, T., Deutscher, N. M., Palm, M., Buschmann, M., Weinzierl, C., Macatangay, R. C., and Grupe, P.: TCCON data from Bremen (DE), Release GGG2014.R0, doi:10.14291/TCCON.GGG2014.BREMEN01.R0/1149275, https://data.caltech.edu/records/268, 2014.

O'Dell, C. W., Connor, B., Boesch, H., O'Brien, D., Frankenberg, C., Castano, R., Christi, M., Crisp, D., Eldering, A., Fisher, B., Gunson, M., McDuffie, J., Miller, C. E., Natraj, V., Oyafuso, F., Polonsky, I., Smyth, M., Taylor, T., Toon, G. C., Wennberg, P. O., and Wunch, D.: The ACOS CO_2 retrieval algorithm - Part 1: Description and validation against synthetic observations, Atmospheric Measurement Techniques, 5, 99–121, 2012.

Pal, S.: ACT-America: Profile-based Planetary Boundary Layer Heights, Eastern USA. ORNL DAAC, Oak Ridge, Tennessee, USA, doi:10.3334/ORNLDAAC/1706, 2019.

Pal, S. and Davis, K.: ACT-America Field Campaign Catalogue. ORNL DAAC, Oak Ridge, Tennessee, USA., https://actamerica.ornl.gov/campaigns.html, 2020.

Pal, S., J., D. K., Lauvaux, T., B. E. V., Gaudet, B. J., and Stauffer, D.: Observations of Greenhouse Gas Changes Across Summer Frontal Boundaries in the Eastern United States, Journal of Geophysical Research -Atmospheres, 125, doi:10.1029/2019JD030526, 2020.

Patra, P. K., Law, R. M., Peters, W., Roedenbeck, C., Takigawa, M., Aulagnier, C., Baker, I., Bergmann, D. J., Bousquet, P., Brandt, J., Bruhwiler, L., Cameron-Smith, P. J., Christensen, J. H., Delage, F., Denning, A. S., Fan, S., Geels, C., Houweling, S., Imasu, R., Karstens, U., Kawa, S. R., Kleist, J., Krol, M. C., Lin, S. J., Lokupitiya, R., Maki, T., Maksyutov, S., Niwa, Y., Onishi, R., Parazoo, N., Pieterse, G., Rivier, L., Satoh, M., Serrar, S., Taguchi, S., Vautard, R., Vermeulen, A. T., and Zhu, Z.: TransCom model simulations of hourly atmospheric CO2: Analysis of synoptic-scale variations for the period 2002-2003, Global Biogeochemical Cycles, 22, doi:10.1029/2007GB003081, gB4013, 2008.

Peterson, J., Komhyr, W., Waterman, L., Gammon, R., Thoning, K., and Conway, T.: Atmospheric CO_2 variations at Barrow, Alaska,1973-1982, Journal of Atmosphere Chemistry, 4, 491–510, doi:10.1007/BF00053848, 1986.

Pillai, D., Gerbig, C., Kretschmer, R., Beck, V., Karstens, U., Neininger, B., and Heimann, M.: Comparing Lagrangian and Eulerian models for CO_2 transport – a step towards Bayesian inverse modeling using WRF/STILT-VPRM, Atmospheric Chemistry and Physics, 12, 8979–8991, doi:10.5194/acp-12-8979-2012, 2012.

Polavarapu, S. M., Neish, M., Tanguay, M., Girard, C., de Grandpré, J., Semeniuk, K., Gravel, S., Ren, S., Roche, S., Chan, D., and Strong, K.: Greenhouse gas simulations with a coupled meteorological and transport model: the predictability of CO_2, Atmospheric Chemistry and Physics, 16, 12 005–12 038, doi:10.5194/acp-16-12005-2016, 2016.

Putman, W. M. and Lin, S.-H.: Finite-volume transport on various cubed-sphere grids, Journal of Computational Physics, 227, 55–78, doi:10.1016/j.jcp.2007.07.022, 2007.

Ramonet, M., Ciais, P., Aalto, T., Aulagnier, C., Chevallier, F., Cipriano, D., Conway, T. J., Haszpra, L., Kazan, V., Meinhardt, F., Paris, J.-D., Schmidt, M., Simmonds, P., Xueref-Remy, I., and Necki, J. N.: A recent build-up of atmospheric CO2 over Europe. Part 1: observed signals and possible explanations, Tellus Series B-Chemical and Physical Meteorology, 62, 1–13, doi:10.1111/j.1600-0889.2009.00442.x, 2010.

Rayner, P. J., Michalak, A. M., and Chevallier, F.: Fundamentals of data assimilation applied to biogeochemistry, Atmospheric Chemistry and Physics, 19, 13 911–13 932, doi:10.5194/acp-19-13911-2019, 2019.

Ringler, T., Ju, L., and Gunzburger, M.: A multiresolution method for climate system modeling: application of spherical centroidal Voronoi tessellations, Ocean Dynamics, 58, 475–498, doi:10.1007/s10236-008-0157-2, 2008.

Ringler, T. D., Thuburn, J., Klemp, J. B., and Skamarock, W. C.: A unified approach to energy conservation and potential vorticity dynamics for arbitrarily-structured C-grids, Journal of Computational Physics, 229, 3065–3090, doi:10.1016/j.jcp.2009.12.007, 2010.

Sarrat, C., Noilhan, J., Lacarrere, P., Donier, S., Lac, C., Calvet, J. C., Dolman, A. J., Gerbig, C., Neininger, B., Ciais, P., Paris, J. D., Boumard, F., Ramonet, M., and Butet, A.: Atmospheric CO2 modeling at the regional scale: Application to the CarboEurope Regional Experiment, Journal of Geophysical Research-Atmospheres, 112, doi:10.1029/2006JD008107, 2007.

Schibig, M. F., Steinbacher, M., Buchmann, B., van der Laan-Luijkx, I. T., van der Laan, S., Ranjan, S., and Leuenberger, M. C.: Comparison of continuous in situ CO_2 observations at Jungfraujoch using two different measurement techniques, Atmospheric Measurement Techniques, 8, 57–68, doi:10.5194/amt-8-57-2015, 2015.

Schmidt, M., Graul, R., Sartorius, H., and Levin, I.: The Schauinsland CO2 record: 30 years of continental observations and their implications for the variability of the European CO2 budget, Journal of Geophysical Research-Atmospheres, 108, doi:10.1029/2002JD003085, 2003.

Schuh, A. E., Lauvaux, T., West, T. O., Denning, A. S., Davis, K. J., Miles, N., Richardson, S., Uliasz, M., Lokupitiya, E., Cooley, D., Andrews, A., and Ogle, S.: Evaluating atmospheric CO2 inversions at multiple scales over a highly inventoried agricultural landscape, Global Change Biology, 19, 1424–1439, doi:10.1111/gcb.12141, 2013.

Schuh, A. E., Jacobson, A. R., Basu, S., Weir, B., Baker, D., Bowman, K., Chevallier, F., Crowell, S., Davis, K. J., Deng, F., Denning, S., Feng, L., Jones, D., Liu, J., and Palmer, I, P.: Quantifying the Impact of Atmospheric Transport Uncertainty on CO2 Surface Flux Estimates, Global Biogeochemical Cycles, 33, 484–500, doi:10.1029/2018GB006086, 2019.

Sherlock, V., Connor, B., Robinson, J., Shiona, H., Smale, D., and Pollard, D. F.: TCCON data from Lauder (NZ), 120HR, Release GGG2014.R0, doi:10.14291/TCCON.GGG2014.LAUDER01.R0/1149293, https://data.caltech.edu/records/280, 2014.

Skamarock, W., Klemp, J., Dudhia, J., Gill, D., Barker, D., Duda, M., Huang, X., Wang, W., and Powers, J.: A description of the Advanced Research WRF version 3, NCAR Tech Note NCAR/TN-475+STR, 2008.

Skamarock, W. C. and Gassmann, A.: Conservative Transport Schemes for Spherical Geodesic Grids: High-Order Flux Operators for ODE-Based Time Integration, Monthly Weather Review, 139, 2962–2975, doi:10.1175/MWR-D-10-05056.1, 2011.

Skamarock, W. C., Klemp, J. B., Duda, M. G., Fowler, L. D., Park, S.-H., and Ringler, T. D.: A Multiscale Nonhydrostatic Atmospheric Model Using Centroidal Voronoi Tesselations and C-Grid Staggering, Monthly Weather Review, 140, 3090–3105, doi:10.1175/MWR-D-11-00215.1, 2012.

Stephens, B. B., Miles, N. L., Richardson, S. J., Watt, A. S., and Davis, K. J.: Atmospheric CO_2 monitoring with single-cell NDIR-based analyzers, Atmospheric Measurement Techniques, 4, 2737–2748, doi:10.5194/amt-4-2737-2011, https://www.atmos-meas-tech.net/4/2737/2011/, 2011.

Sussmann, R. and Rettinger, M.: TCCON data from Garmisch (DE), Release GGG2014.R0, doi:10.14291/TCCON.GGG2014.GARMISCH01.R0/1149299, https://data.caltech.edu/records/273, 2015.

Thoning, K., Tans, P., and Komhyr, W.: Atmospheric carbon dioxide at Mauna Loa Observatory, 2. Analysis of the NOAA/GMCC data, 1974-1985, Journal of Geophysical Research-Atmospheres, 94, 8549–8565, doi:10.1029/JD094iD06p08549, 1989.

Thuburn, J.: Rossby wave dispersion on the C-grid, Atmospheric Science Letters, 8, 37–42, doi:10.1002/asl.148, 2007.

Tsutsumi, Y., Matsueda, H., and Nishioka, S.: Consistency of the CO2 primary standards in JMA, 12th WMO/IAEA meeting of experts on carbon dioxide concentration and related tracers measurement techniques (Toronto, Canada, 15– 18 September 2003), Global Atmosphere Watch Report No. 161 (WMO/TD-No.1275), 2005.

Vermeulen, A. T., Hensen, A., Popa, M. E., van den Bulk, W. C. M., and Jongejan, P. A. C.: Greenhouse gas observations from Cabauw Tall Tower (1992–2010), Atmospheric Measurement Techniques, 4, 617–644, doi:10.5194/amt-4-617-2011, https://www.atmos-meas-tech.net/4/617/2011/, 2011.

Walko, R. L. and Avissar, R.: The Ocean-Land-Atmosphere Model (OLAM). Part I: Shallow-Water Tests, Monthly Weather Review, 136, 4033–4044, doi:10.1175/2008MWR2522.1, 2008a.

Walko, R. L. and Avissar, R.: The Ocean-Land-Atmosphere Model (OLAM). Part II: Formulation and Tests of the Nonhydrostatic Dynamic Core, Monthly Weather Review, 136, 4045–4062, doi:10.1175/2008MWR2523.1, 2008b.

Warneke, T., Messerschmidt, J., Notholt, J., Weinzierl, C., Deutscher, N. M., Petri, C., and Grupe, P.: TCCON data from Orléans (FR), Release GGG2014.R0, doi:10.14291/TCCON.GGG2014.ORLEANS01.R0/1149276, https://data.caltech.edu/records/283, 2014.

Wennberg, P. O., Roehl, C. M., Wunch, D., Toon, G. C., Blavier, J.-F., Washenfelder, R., Keppel-Aleks, G., Allen, N. T., and Ayers, J.: TCCON data from Park Falls (US), Release GGG2014.R0, doi:10.14291/TCCON.GGG2014.PARKFALLS01.R0/1149161, https://data.caltech.edu/records/204, 2014a.

Wennberg, P. O., Wunch, D., Roehl, C. M., Blavier, J.-F., Toon, G. C., Allen, N. T., Dowell, P., Teske, K., Martin, C., and Martin, J.: TCCON data from Lamont (US), Release GGG2014.R0, doi:10.14291/TCCON.GGG2014.LAMONT01.R0/1149159, https://data.caltech.edu/records/262, 2014b.

Williamson, D.: Semi-Lagrangian moisture transport in the NMC spectral model, Tells A: Dynamic Meteorology and Oceanography, 42, 413–428, doi:10.3402/tellusa.v42i4.11887, 1990.

Wilson, P.: Insight into the Carbon Cycle from Continuous Measurements of Oxygen and Carbon Dioxide at Weybourne Atmospheric Observatory, UK,, PhD thesis, University of East Anglia, Norwich, UK, 2013.

Worthy, D., Higuchi, K., and Chan, D.: North American influence on atmospheric carbon dioxide data collected at Sable Island, Canada, Tellus Series B-Chemical anD Physical Meteorology, 55, 105–114, doi:10.1034/j.1600-0889.2003.00051.x, 2003.

Wunch, D., Toon, G. C., Wennberg, P. O., Wofsy, S. C., Stephens, B. B., Fischer, M. L., Uchino, O., Abshire, J. B., Bernath, P., Biraud, S. C., Blavier, J. F. L., Boone, C., Bowman, K. P., Browell, E. V., Campos, T., Connor, B. J., Daube, B. C., Deutscher, N. M., Diao, M., Elkins, J. W., Gerbig, C., Gottlieb, E., Griffith, D. W. T., Hurst, D. F., Jimenez, R., Keppel-Aleks, G., Kort, E. A., Macatangay, R., Machida, T., Matsueda, H., Moore, F., Morino, I., Park, S., Robinson, J., Roehl, C. M., Sawa, Y., Sherlock, V., Sweeney, C., Tanaka, T., and Zondlo, M. A.: Calibration of the Total Carbon Column Observing Network using aircraft profile data, Atmospheric Measurement Techniques, 3, 1351–1362, 2010.

Zheng, T., Nassar, R., and Baxter, M.: Estimating power plant CO_2 emission using OCO-2 XCO_2 and high resolution WRF-Chem simulations, Environmental Research Letters, 14, doi:10.1088/1748-9326/ab25ae, 2019.

Zheng, T., French, N. H. F., and Baxter, M.: Development of the WRF-CO_2 4D-Var assimilation system v1.0, Geoscientific Model Development, 11, 1725–1752, doi:10.5194/gmd-11-1725-2018, 2018.

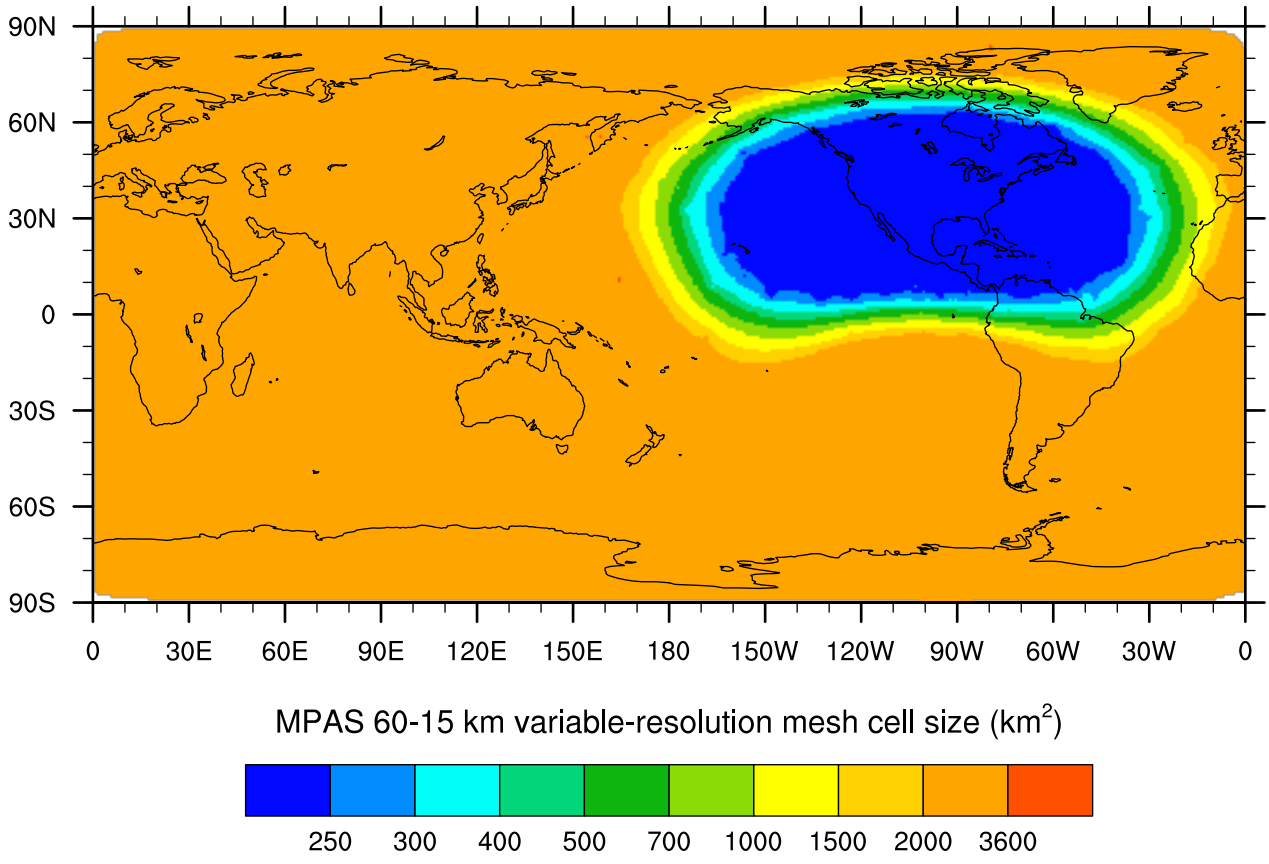

Figure 1. Variable-resolution 60-15 km global domain for MPAS-A CO_2 simulations conducted for model evaluation using aircraft and near-surface CO_2 observations. The highest resolution (15 km) grid covering the most of the North America has cell size less than 250 km^2. The cell sizes (represented by color) gradually increase to about 3,600 km^2 for the rest of the global domain.

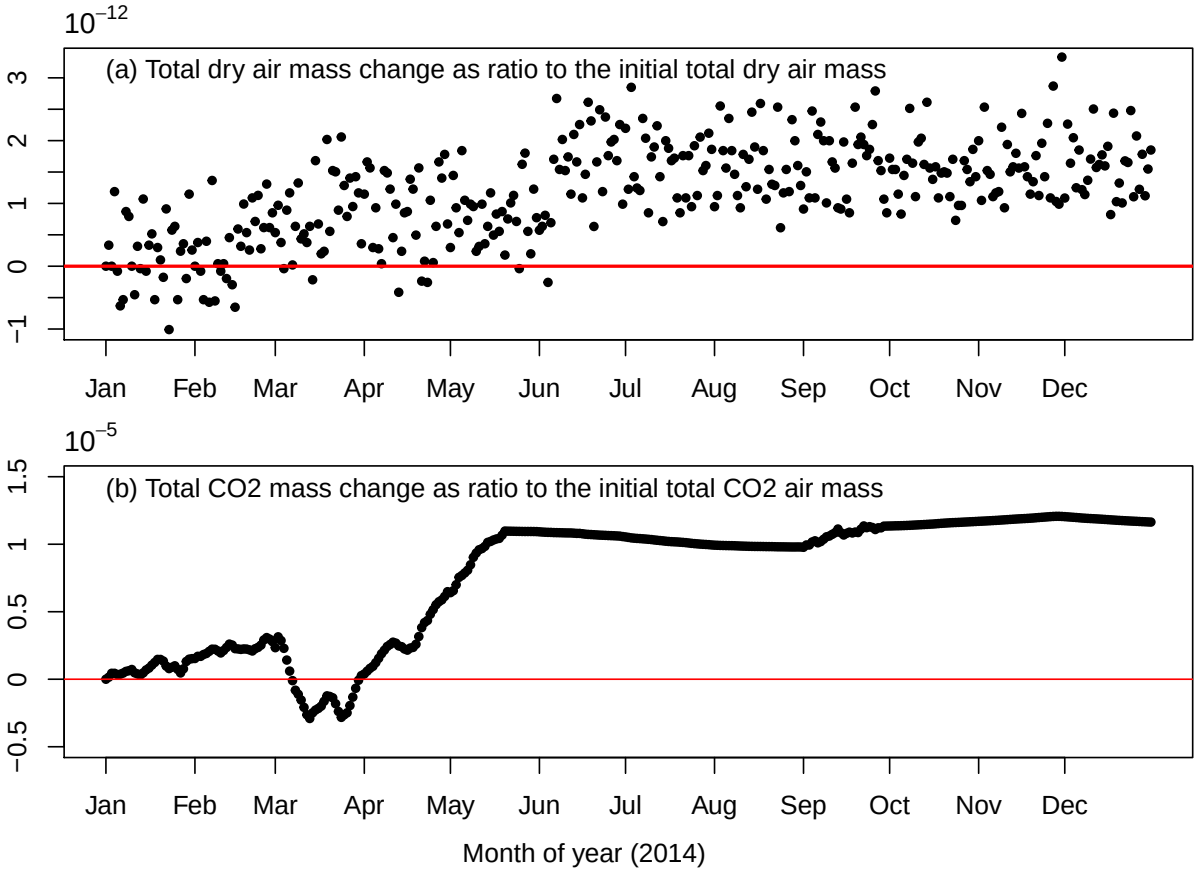

Figure 2. Variation of total dry air mass (a) and total CO_2 mass (b) as the ratio to their respective starting values during a 1-year continuous MPAS-A simulation without meteorological re-initialization. The X-axis represents the number of hours after the start of the simulation, and the Y-axis the ratio of the total mass change to the starting values.

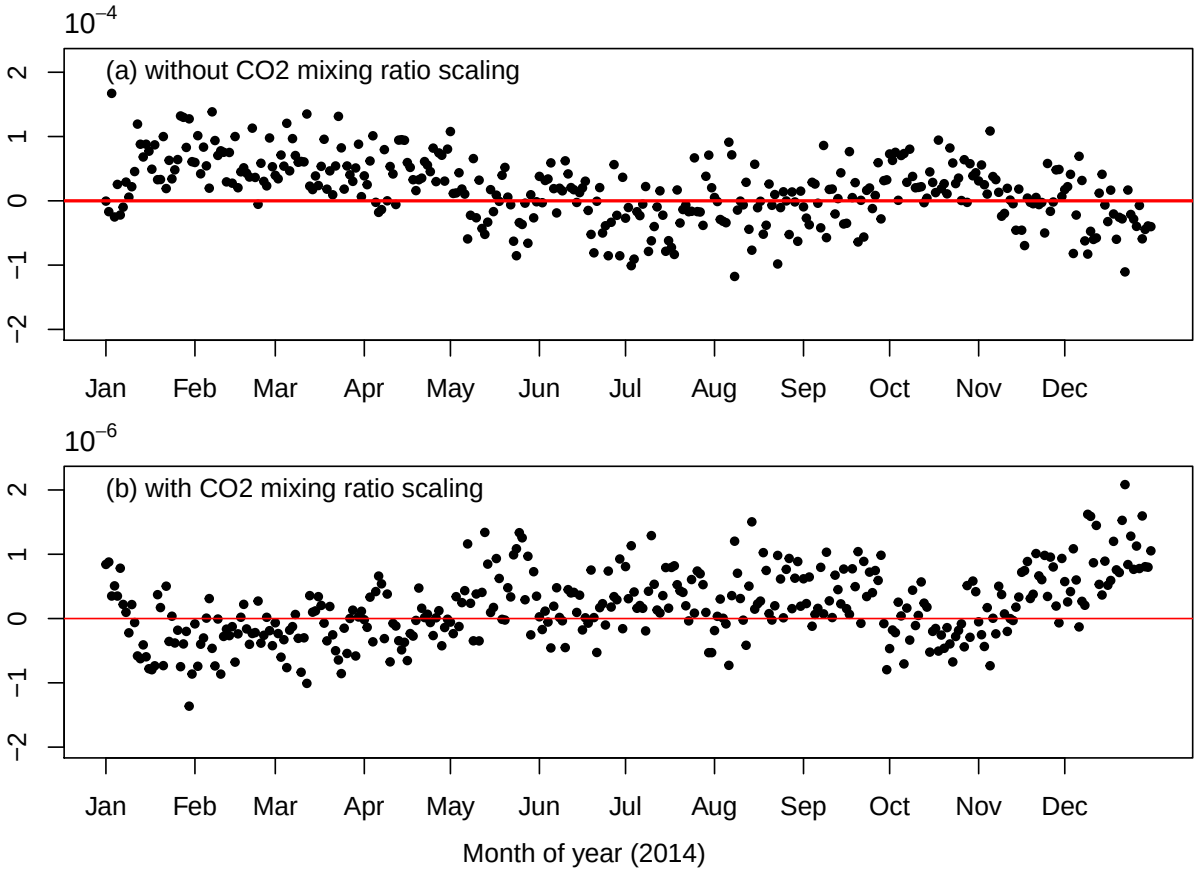

Figure 3. Variation of global CO_2 mass as the ratio to its value prior to a meteorological re-initialization during a 1-year MPAS-A simulation with meteorological re-initializations at 24-hour intervals. The top figure is from the simulation without applying CO_2 mixing ratio scaling as described in Sect. 3.2.2, and the bottom figure is from the simulation with the scaling. In each figure, X-axis represents the number of days after the start of the simulation, and Y-axis the ratio of global CO_2 mass variation to its value prior to a meteorological re-initialization.

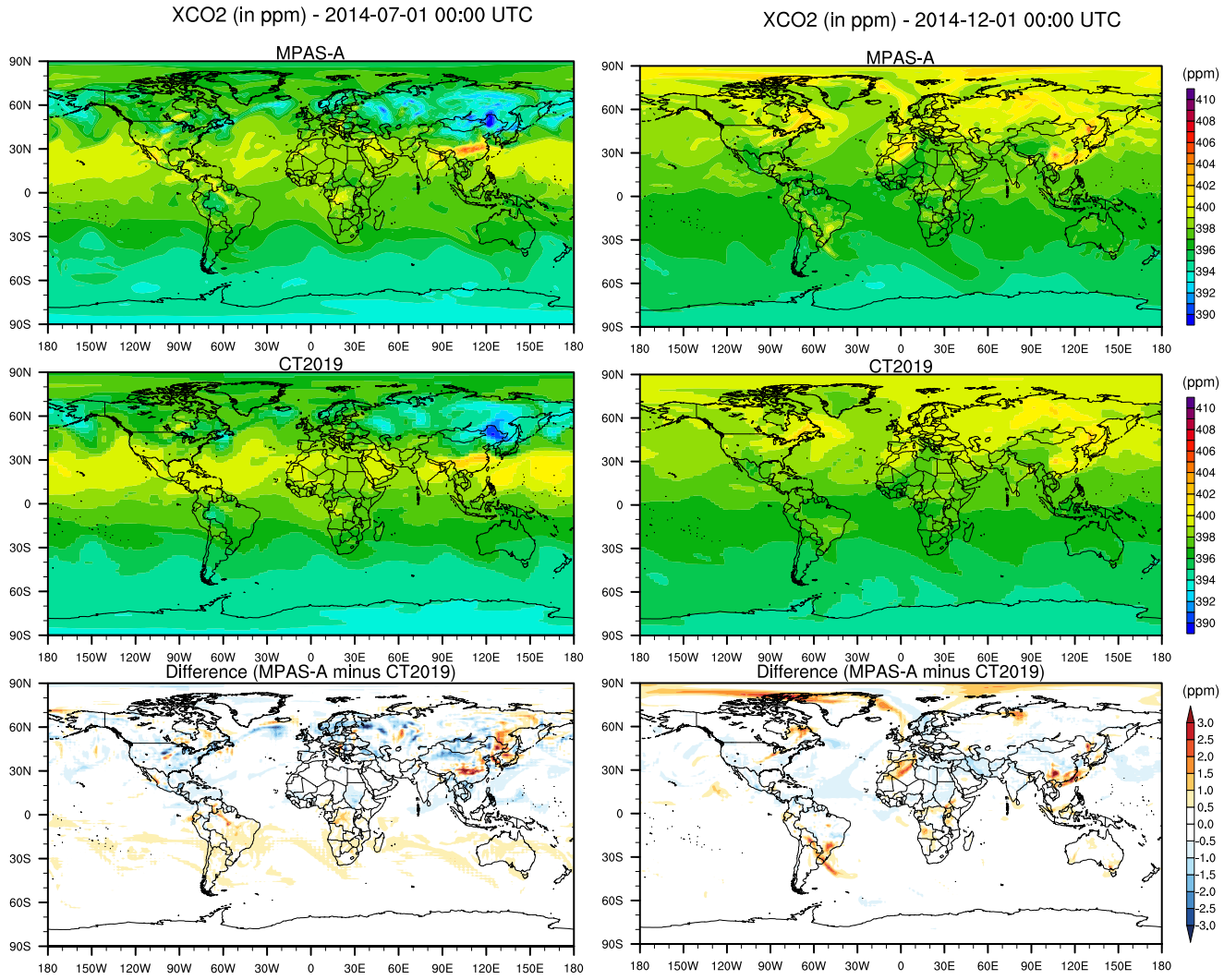

Figure 4. XCO_2 of MPAS-A, CT2019, and their difference at 2014-07-01 and 2014-12-01 00:00 UTC.

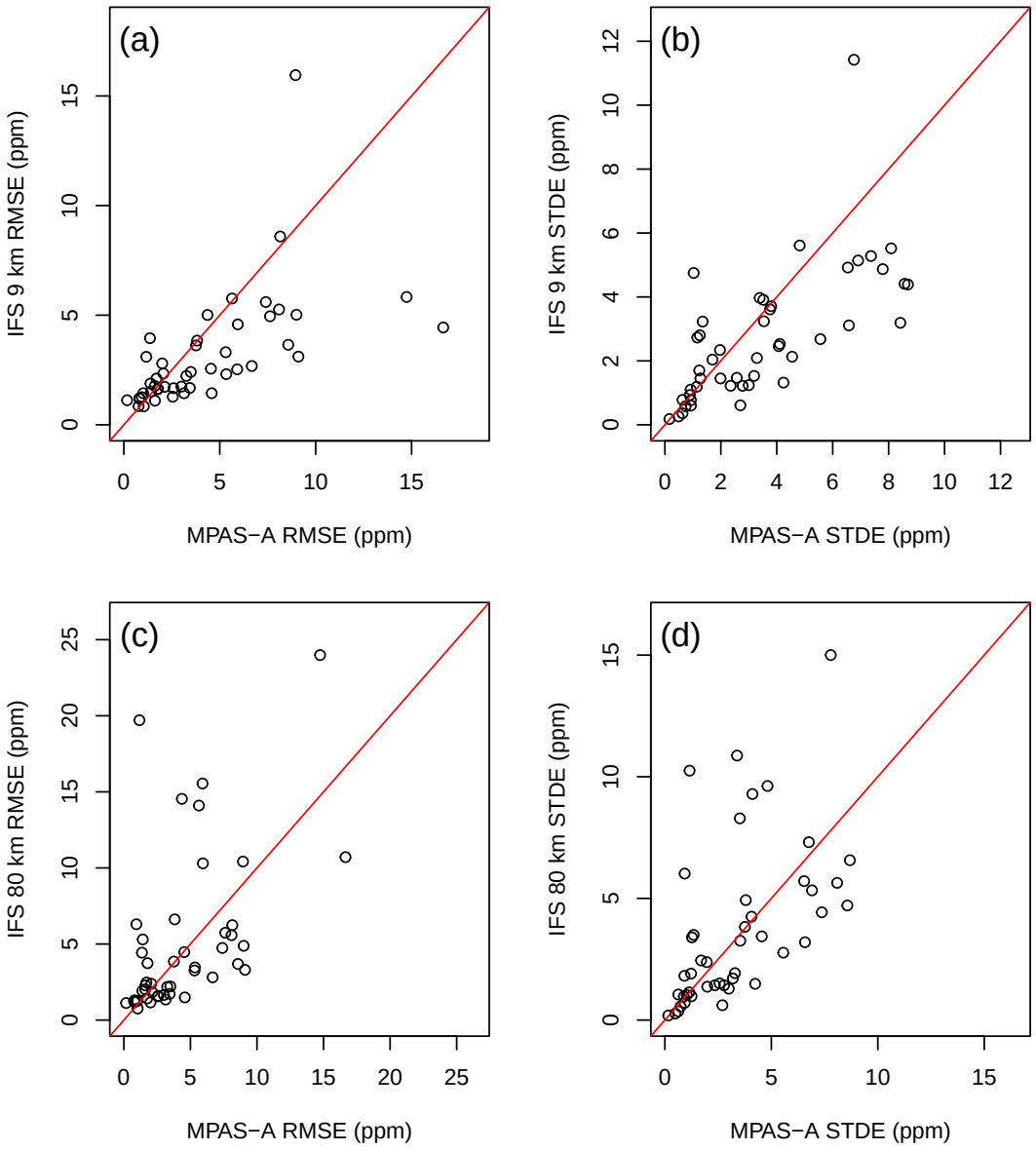

Figure 5. Comparison of model simulated hourly CO_2 accuracy (RMSE and STDE) between MPAS-A and IFS at 50 surface and tower stations. Each open circle in the figures represent a station. Comparison of MPAS-A with the IFS 9 km resolution simulations are in the top panel (a and b), and comparison with IFS 80 km resolutions simulations are in the top panel (c and d).

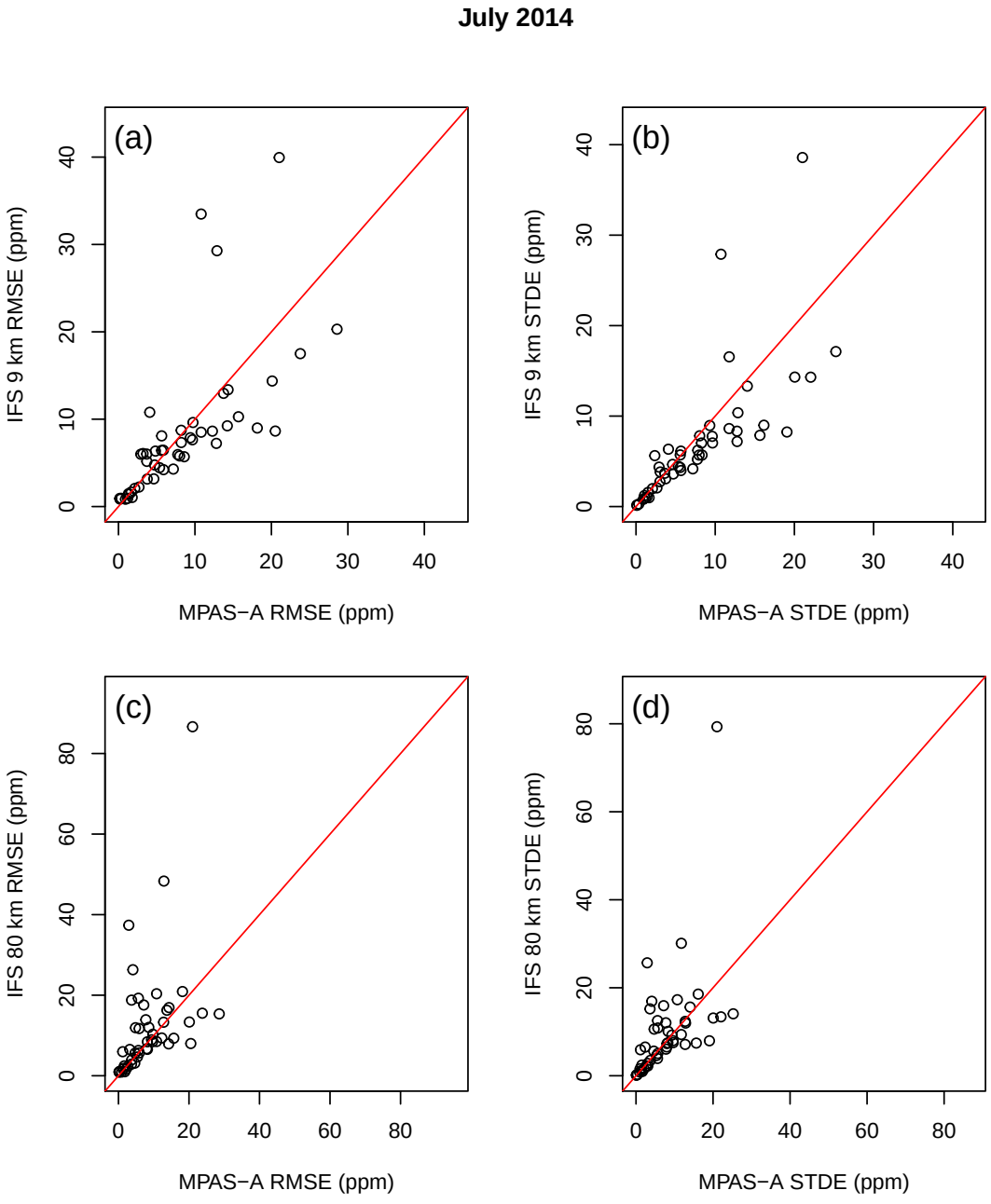

Figure 6. Same as Fig. 5, but for the month of July 2014

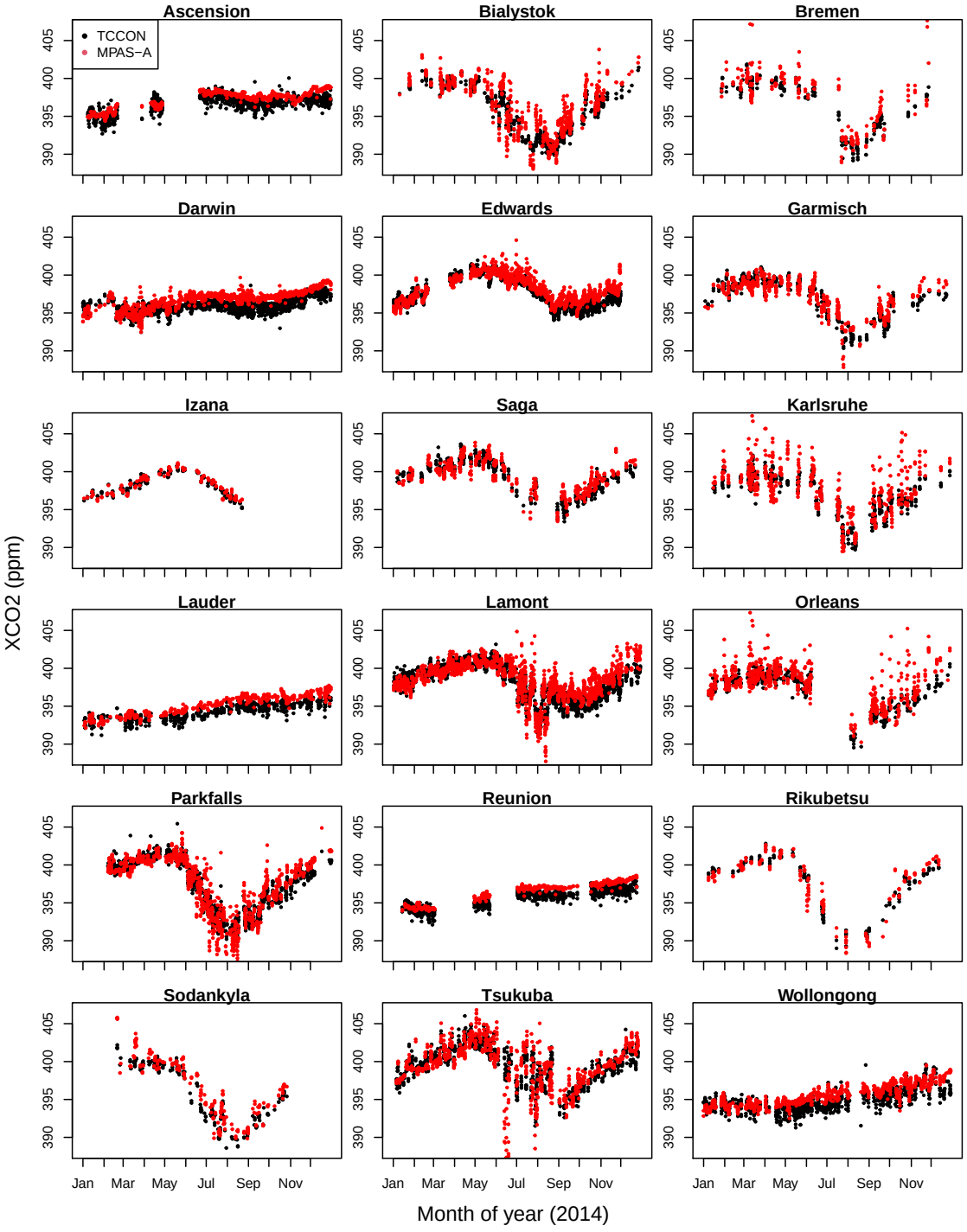

Figure 7. MPAS-A simulated hourly XCO_2 at 18 TCCON sites for the year of 2014

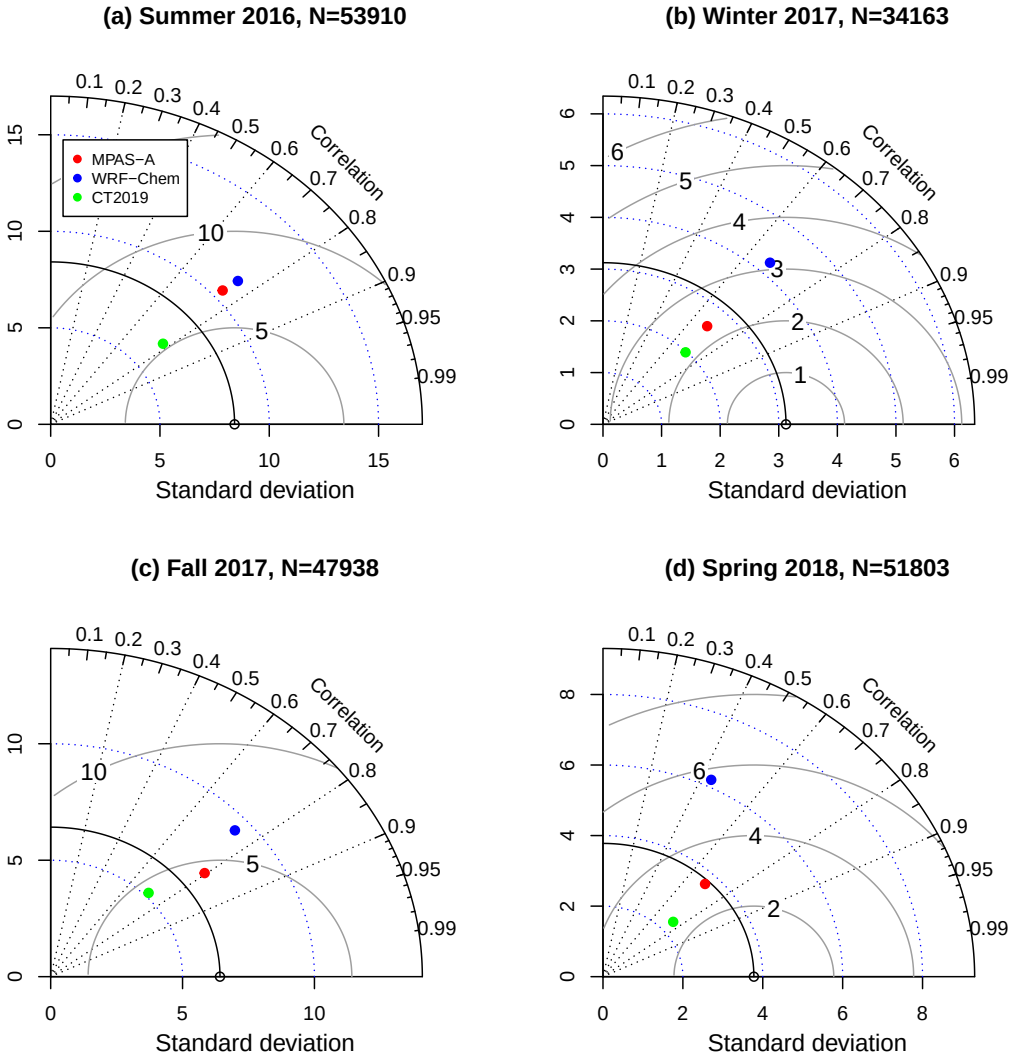

Figure 8. Taylor diagram for model evaluation using ACT airborne measurements in the boundary layer.

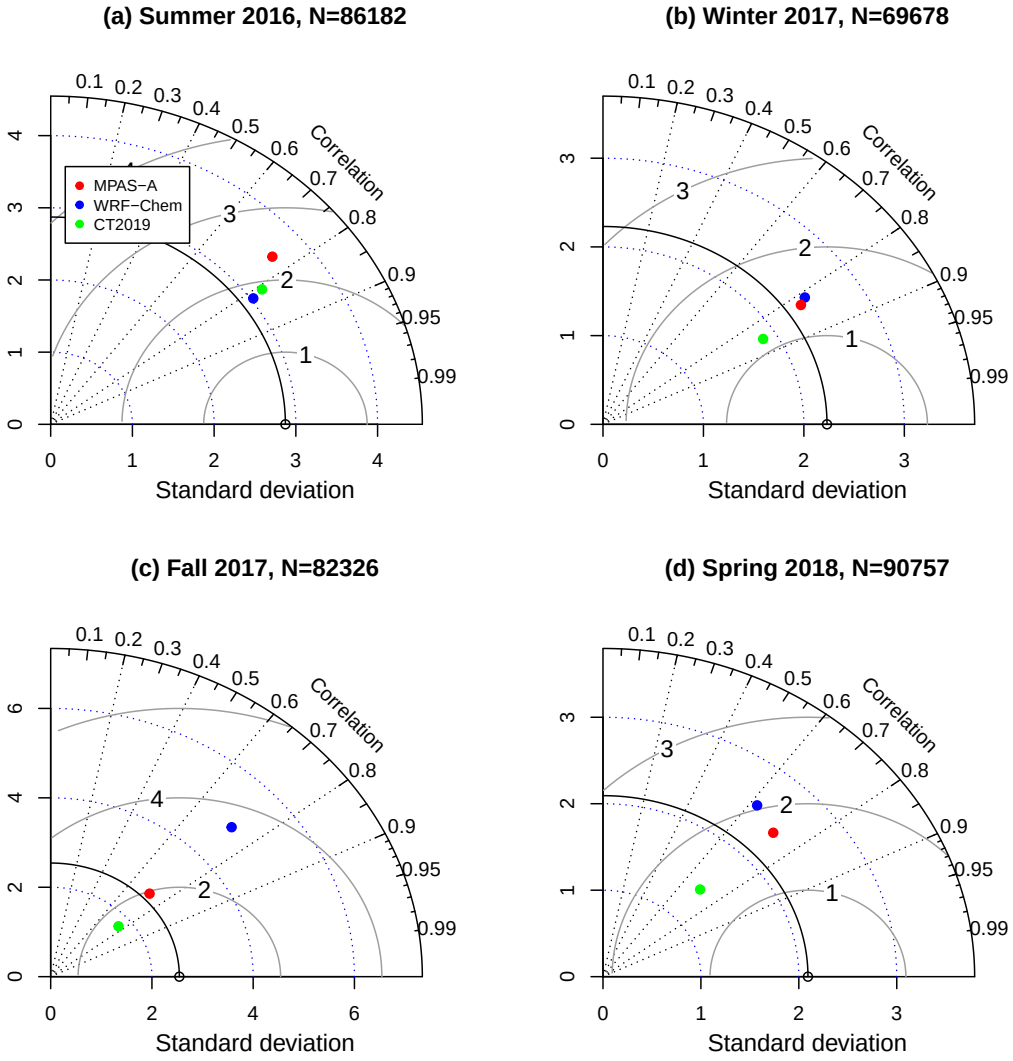

Figure 9. Taylor diagram for model evaluation using ACT airborne measurements in the free troposphere.

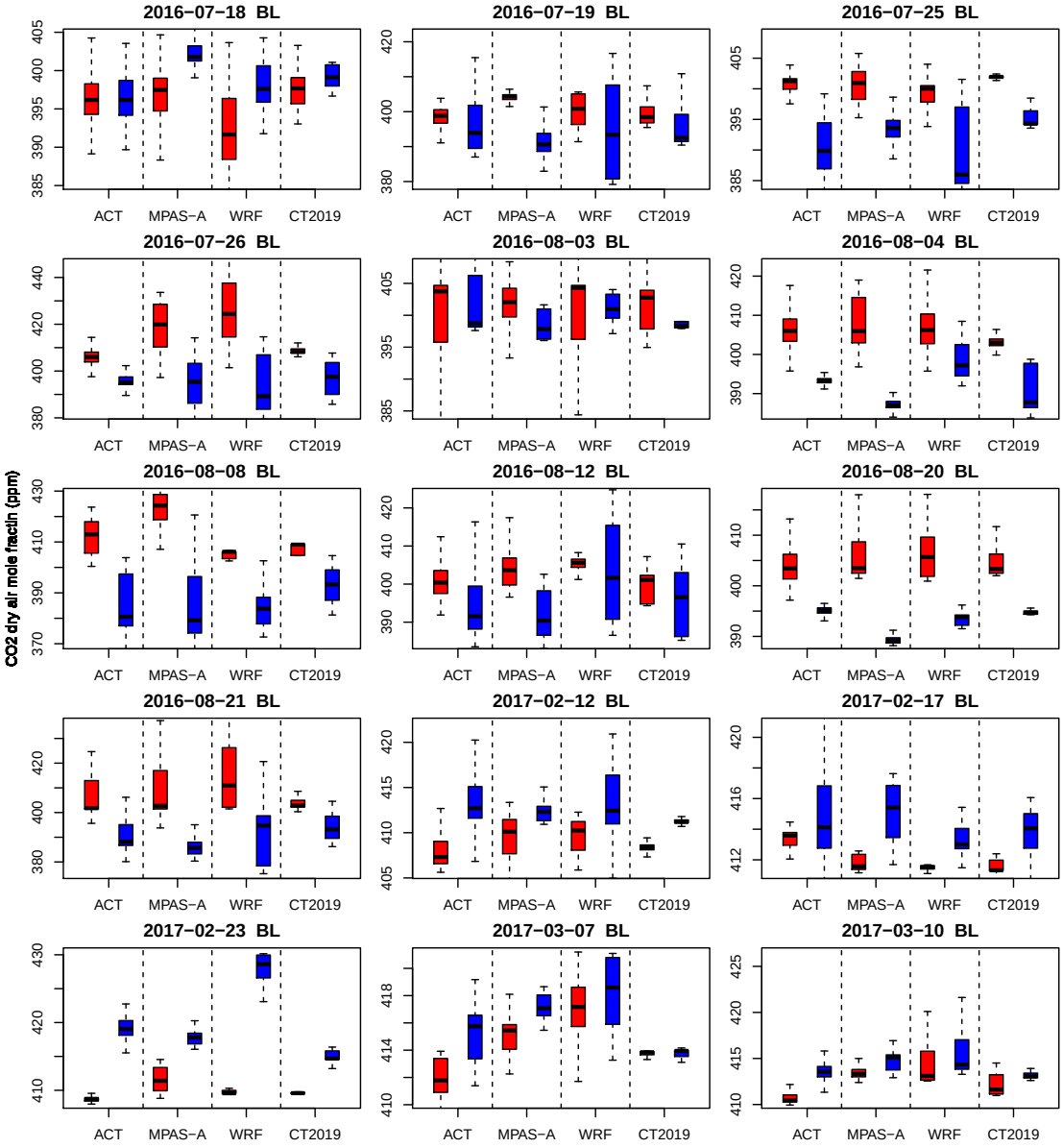

Figure 10. Box plots comparing mean boundary layer (BL) CO_2 mole fraction of the warm sector (red color) and cold sector (blue color) for 15 frontal crossing flights from summer 2016 and winter 2017 ACT campaign seasons. The flight date of each plot is labeled in its title. Data are combined when both aircraft (C130 and B200) took measurements for a given day. Each sub-figure is separated into four groups by the dotted lines: the first group is from ACT observations, the second is MPAS-A simulation, the third is WRF-Chem simulation, and the last is CT2019. In each boxplot, the bottom and top edge of the box represent the 1^{st} (Q1) and $3^{rd}(Q3)$ quartiles, the horizontal line represent the median, the ends of the whisker represents Q1-1.5×IQR and Q3+1.5×IQR respectively, where IQR=Q3-Q1.

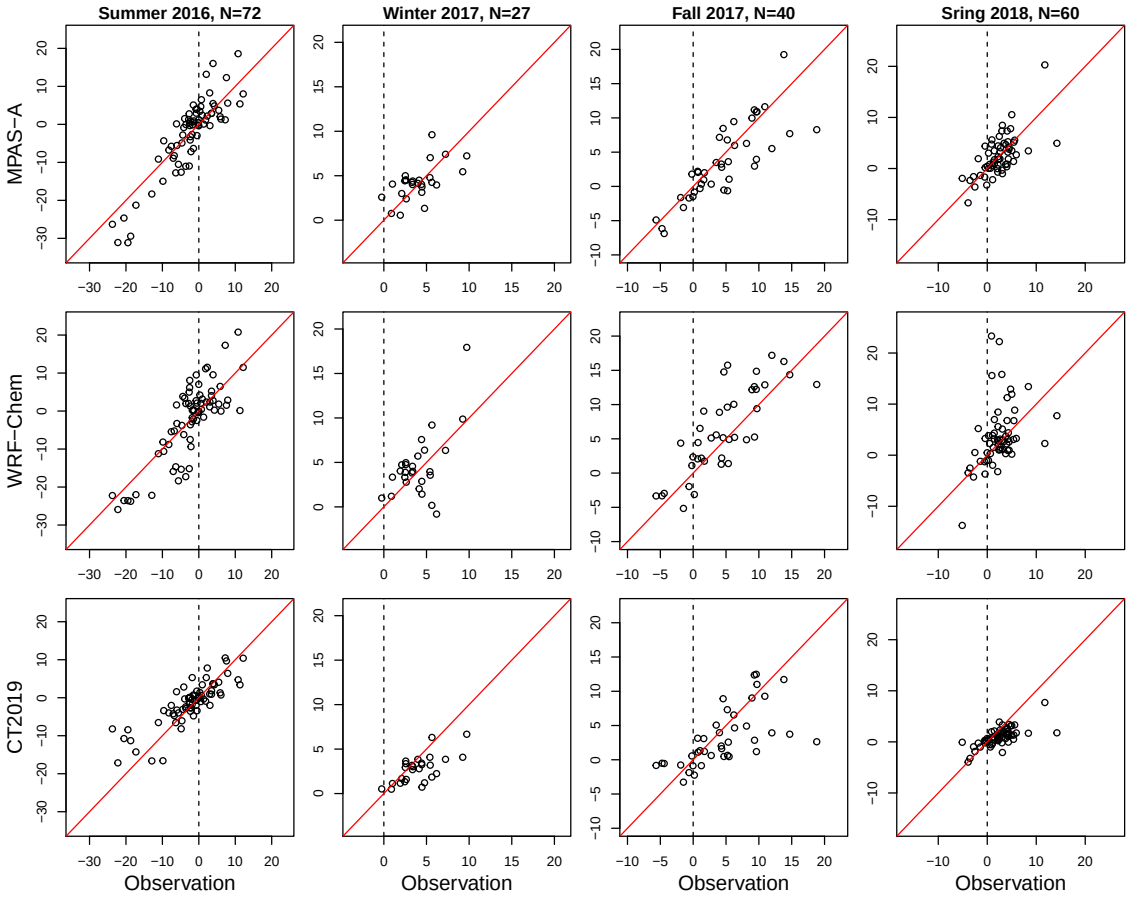

Figure 11. The difference of mean CO_2 mole fraction between boundary layer (BL) and free troposphere (FT) ($\Delta[CO_2] = [CO_2]_{BL} - [CO_2]_{FT}$) at vertical profiling flight legs. In each subplot, each open circle represents an individual vertical profiling flight leg, and its values on the X-axis and Y-axis represent its $\Delta[CO_2]$ value from the aircraft observations and the model simulation respectively. $\Delta[CO_2]$ from MPAS-A simulations are the first row, WRF-Chem the second row, and CT2019 the third. The four columns in the figure are for the four ACT campaign seasons. The number of vertical profiles in each season is labeled in the column title. The vertical dashed line marks where $\Delta[CO_2] = 0$ based on the aircraft measurements.

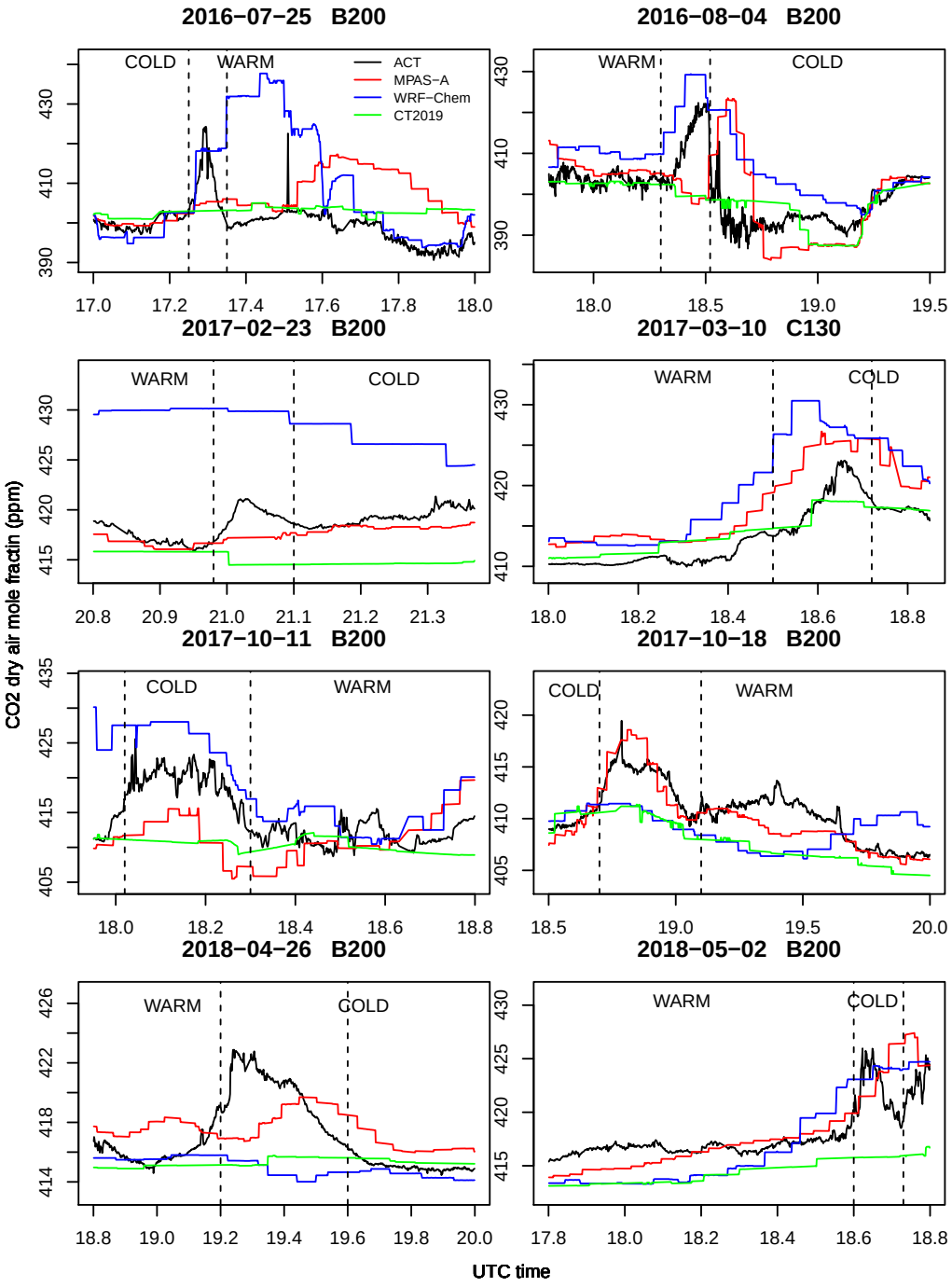

Figure 12. Comparison of CO_2 mole fraction in frontal-crossing level-leg flights in boundary layer between ACT aircraft measurements and model simulations. Flight date and aircraft type are labeled in title for each flight leg. X-axis is UTC time, and Y-axis is CO_2 mole fraction (ppm). Aircraft measurements are in black, MPAS-A in red, WRF-Chem in blue, and CT2019 in green. In each figure, the pair of vertical dashed lines mark CO_2 enhancement observed by the aircraft along a frontal boundary, and the warm and cold sectors associated with the frontal boundary are labeled as warm and cold, respectively.

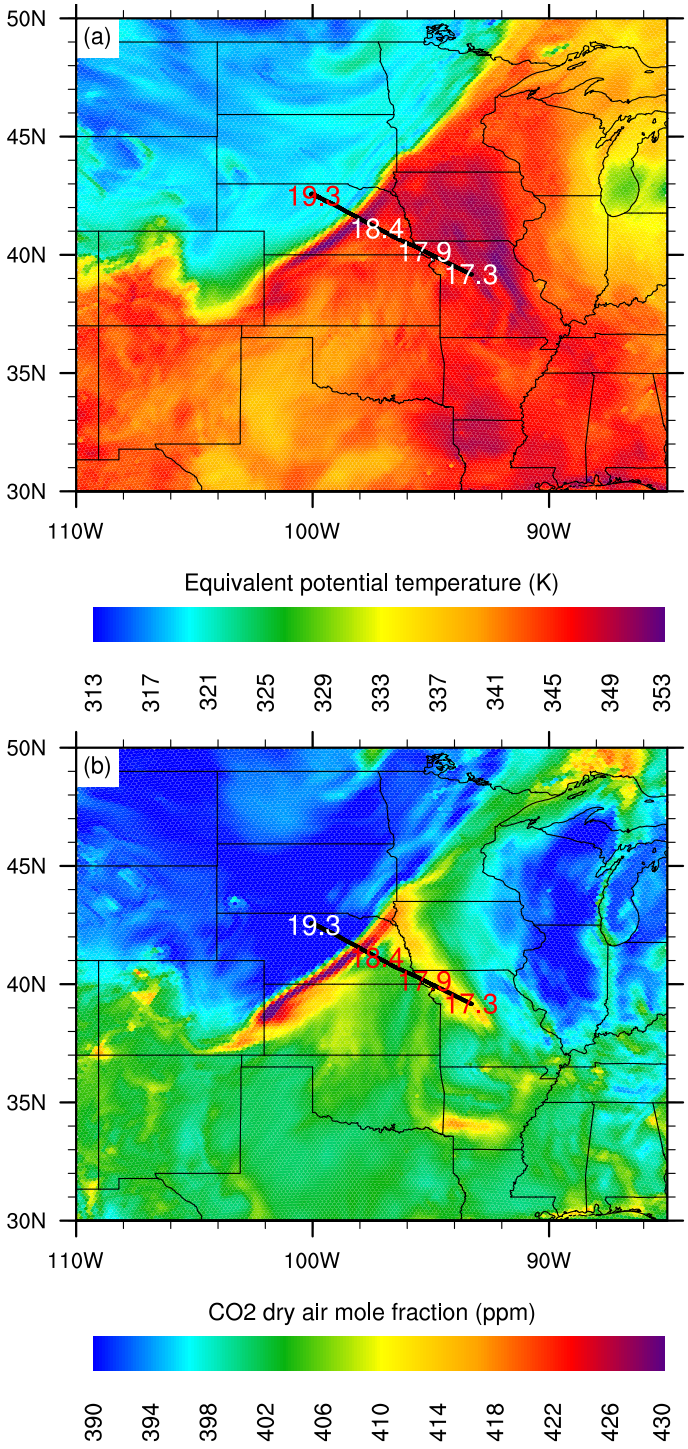

Figure 13. MPAS-A simulated equivalent potential temperature (θ_e, top panel) and CO_2 mole fraction (bottom panel) at 18:00 UTC 4 August 2016. Both figures are plotted at MPAS-A 6^{th} vertical level, which is about 400 meters above the ground.

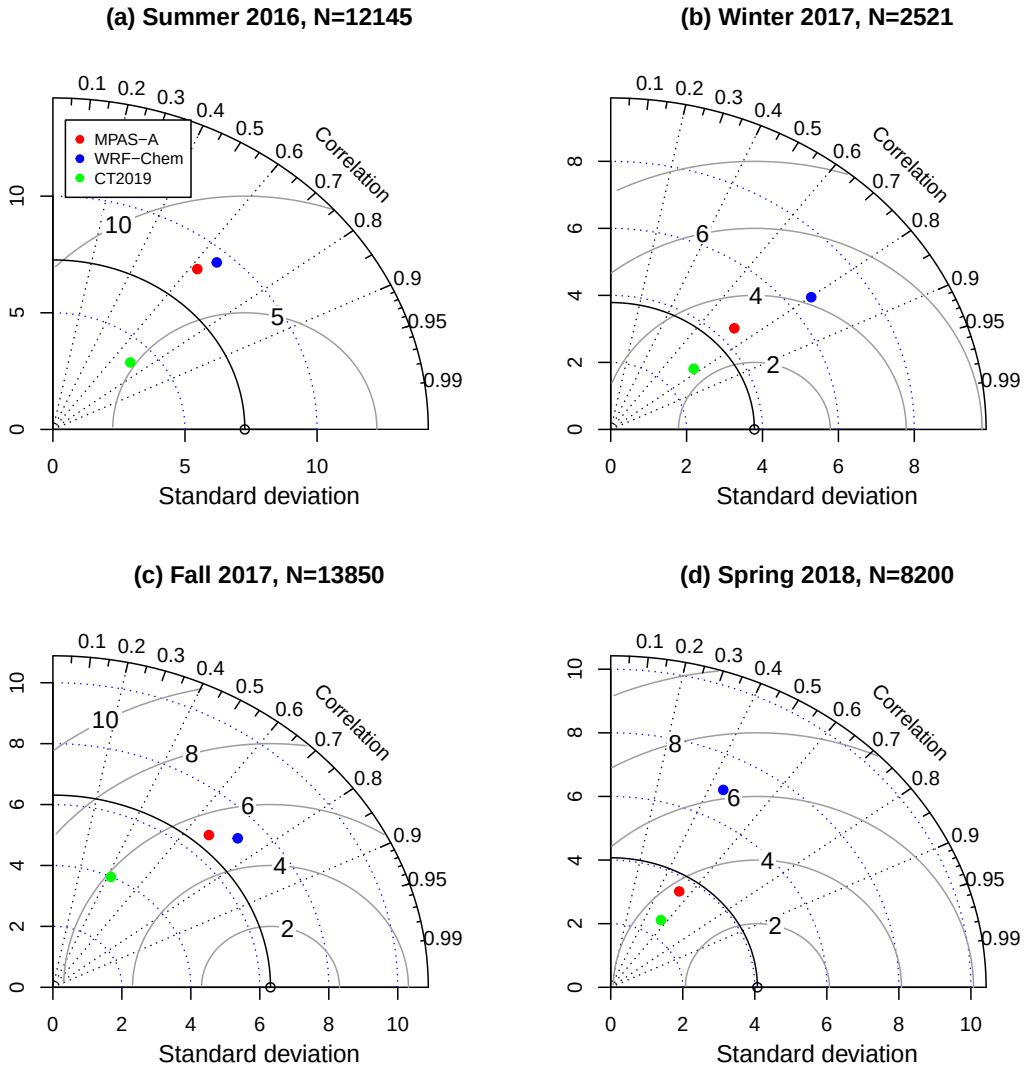

Figure 14. Taylor diagram for model evaluation using ACT airborne measurements from front-crossing flights. For each of the four ACT campaign seasons, observation-model data pairs from all front-crossing flights are combined. N is the number of data pairs of used for create the diagram.

Table 1. MPAS-A CO_2 transport model simulation physical parameterizations summary.

Parameterization	Option Used	References
Longwave	RRTMG LW	Iacono et al. (2008)
Shortwave	RRTMG SW	Iacono et al. (2008)
PBL	YSU	Hong et al. (2006)
Surface layer	Monin-Obukhov	
Land Surface Model	Noah	Chen and Dudhia (2001)
Cumulus	Kain-Fritsch	Kain (2004)
Microphysics	WRF Single Moment 6-class	Hong and Lim (2006)

Table 2. Evaluation of MPAS-A simulated horizontal wind using NOAA IGRA radiosonde data. Radiosonde data from 457 stations over the globe are used for the evaluation. Wind speed and direction are compared at 00:00 UTC and 12:00 UTC at four pressure levels (1000, 850, 500, and 200 hPa) for each day of the MPAS-A simulation. The number of data samples (N) are smaller at 1000 hPa because some stations are located above that pressure level.

	Pressure level	Mean RMSE vector wind (m/s)	Bias Wind speed (m/s)	Mean difference Wind direction °	Number of data
January 2014	1000 hPa	3.83	0.89	31.00	8,856
	850 hPa	4.04	-0.45	23.08	22,369
	500 hPa	3.72	-0.50	12.98	23,222
	200 hPa	4.38	-0.58	8.36	22,795
July 2014	1000 hPa	3.47	0.27	32.94	7,504
	850 hPa	3.56	-0.51	27.12	22,832
	500 hPa	3.39	-0.59	17.89	23,745
	200 hPa	4.19	-0.55	12.19	23,455

Table 3. The statistics of MPAS-A simulated horizontal wind validated at radiosonde stations located in North America. In each cell, the first value is from the 60-15 km variable-resolution grid simulation (labeled as 15 km) and the second is from the 60 km uniform grid simulation (labeled as 60 km). Note that the number of data at the 850 hPa and 1000 hPa are different between the two simulations because of the differences in their grids' topography.

	Pressure level	Mean RMSE vector wind (m/s) 15 km / 60 km	Bias Wind speed(m/s) 15 km / 60 km	Mean difference Wind direction ° 15 km / 60 km	Number of data 15 km / 60 km
January 2014	1000 hPa	3.46 / 3.98	0.84 / 1.02	30.27 / 32.24	2,427 / 1,845
	850 hPa	3.42 / 4.08	-0.32 / -0.59	21.58 / 24.70	6,227 / 6,187
	500 hPa	3.37 / 3.68	-0.41 / -0.54	13.10 / 13.89	6,659 / 6,659
	200 hPa	4.01 / 4.20	-0.44 / -0.53	8.54 / 8.78	6,536 / 6,536
July 2014	1000 hPa	3.10 / 3.64	0.13 / 0.39	32.91 / 33.93	2,778 / 2,027
	850 hPa	3.34 / 4.08	-0.35 / -0.60	26.08 / 27.66	6,395 / 6,321
	500 hPa	3.26 / 3.68	-0.54 / -0.65	17.46 / 18.25	6,861 / 6,861
	200 hPa	3.76 / 4.06	-0.41 / -0.40	10.99 / 11.70	6,808 / 6,808

Table 4. Continuous in-situ stations used for evaluating MPAS-A CO_2 simulation accuracy. NA denotes references that are not available.

Station ID	Latitude	longitude	altitude (m a.m.s.l)	intake (m a.g.l)	Reference	Type
ALT	82.45 N	62.51 W	200	10	Worthy et al. (2003)	remote
BRW	71.32 N	156.61 W	11	16	Peterson et al. (1986)	coastal
CBY	69.13 N	105.06 W	35	12	NA	continental
INU	68.32 N	133.53 W	113	10	Worthy et al. (2003)	continental
PAL	67.97 N	24.12 E	560	5	Hatakka et al. (2003)	continental
BCK	62.80 N	116.05 W	179	60	NA	continental
CHL	58.74 N	94.07 W	29	60	Worthy et al. (2003)	coastal
LLB	54.95 N	112.45 W	540	10	Worthy et al. (2003)	continental
ETL	54.35 N	104.99 W	492	105	Worthy et al. (2003)	continental
MHD	53.33 N	9.90 W	5	24	Ramonet et al. (2010)	coastal
WAO	52.95 N	1.12 E	20	10	Wilson (2013)	coastal
CES	51.97 N	4.93 E	-1	207	Vermeulen et al. (2011)	continental
EST	51.66 N	110.21 W	707	3	Worthy et al. (2003)	continental
FSD	49.88 N	81.57 W	210	40	Worthy et al. (2003)	continental
CPS	49.82 N	74.98 W	381	8	Worthy et al. (2003)	continental
ESP	49.38 N	126.54 W	7	40	Worthy et al. (2003)	coastal
KAS	49.23 N	19.98 E	1989	5	Necki et al. (2003)	mountain
SSL	47.92 N	7.92 E	1205	12	Schmidt et al. (2003)	mountain
HUN	46.95 N	16.65 E	248	115	Haszpra et al. (2001)	continental
JFJ	46.55 N	7.99 E	3570	10	Schibig et al. (2015)	mountain
LEF	45.95 N	90.27 W	472	396	Andrews et al. (2014)	continental
PUY	45.77 N	2.97 E	1465	10	Lopez et al. (2015)	mountain
AMT	45.03 N	68.68 W	53	107	Andrews et al. (2014)	continental
EGB	44.23 N	79.78 W	251	3	Worthy et al. (2003)	continental
WSA	43.93 N	60.01 W	5	25	Worthy et al. (2003)	remote
VAC	42.88 N	3.21 W	1086	20	Morgui et al. (2013)	mountain
TPD	42.64 N	80.56 W	231	35	Worthy et al. (2003)	continental
DEC	40.74 N	0.79 E	1	10	Morgui et al. (2013)	coastal
HDP	40.56 N	111.65 W	3351	17.7	Stephens et al. (2011)	mountain
SPL	40.45 N	106.73 W	3210	9.1	Stephens et al. (2011)	mountain
GIC	40.35 N	5.18 W	1436	20	Morgui et al. (2013)	mountain
NWR	40.05 N	105.59 W	3523	3.5	Stephens et al. (2011)	mountain
BAO	40.05 N	105.00 W	1584	300	Andrews et al. (2014)	continental
RYO	39.03 N	141.82 E	260	20	Tsutsumi et al. (2005)	coastal
SNP	38.62 N	78.35 W	1008	17	Andrews et al. (2014)	mountain
WGC	38.26 N	121.49 W	0	483	Andrews et al. (2014)	coastal
SGC	36.70 N	5.38 W	850	20	Morgui et al. (2013)	continental
SCT	33.41 N	81.83 W	115	305	Andrews et al. (2014)	continental

Table 4. - Continued from previous page

Station ID	Latitude	longitude	altitude (m a.m.s.l)	intake (m a.g.l)	Reference	Type
WKT	31.31 N	97.33 W	251	457	Andrews et al. (2014)	continental
IZO	28.31 N	16.50 W	2373	13	Gomez-Pelaez and Ramos (2005)	mountain
YON	24.47 N	123.01 E	30	20	Tsutsumi et al. (2005)	coastal
MNM	24.29 N	153.98 E	8	20	Tsutsumi et al. (2005)	remote
MLO	19.54 N	155.58 W	3397	40	Thoning et al. (1989)	mountain
SMO	14.25 S	170.56 W	42	10	Halter et al. (1988)	remote
CPT	34.35 S	18.49 E	230	30	Brunke et al. (2004)	coastal
AMS	37.80 S	77.54 E	55	20	Gaudry et al. (1991)	remote
CGO	40.68 S	144.69 E	94	70	Francey et al. (2003)	coastal
CYA	66.28 S	110.52 E	47	7	Loh et al. (2017)	remote
SYO	69.00 S	39.58 E	14	8	NA	remote
SPO	89.98 S	24.80 W	2810	10	Conway and Thoning (1990)	remote

Table 5. Comparison of Mean RMSE of hourly CO_2 from MPAS-A and IFS 9 km and 80 km simulations. p-value of paired t test between MPAS-A and the IFS simulations are also listed.

		Mean RMSE			p value of paired t-test	
	Number of data	MPAS-A	IFS 9km	IFS 80 km	MPAS-A vs IFS 9 km	MPAS-A vs IFS 80 km
January 2014	50	4.20	3.12	4.94	0.01	0.25
July 2014	50	8.09	8.04	11.77	0.95	0.04

Table 6. Comparison of RMSE of hourly CO_2 between the MPAS-A 60-15 km simulation and the IFS 9 km and 80 km simulations at 12 mountain sites (Table 4). The left half of the table is for six mountain sites located in MPAS-A's 15 km cells and the second half is for six mountain sites located in MPAS-A's 60 km cells. The top half of the table is for January 2014 and the bottom half is for July 2014.

	Sites at MPAS-A 15 km cells RMSE				Sites at MPAS-A 60 km cells RMSE			
	Site	IFS 9km	IFS 80 km	MPAS-A	Site	IFS 9km	IFS 80 km	MPAS-A
January 2014	HDP	3.10	19.71	1.17	KAS	4.44	10.71	16.65
	SPL	3.95	4.43	1.36	SSL	5.83	23.99	14.74
	NWR	1.64	3.74	1.78	JFJ	2.53	15.55	5.91
	SNP	5.01	14.54	4.36	PUY	4.58	10.30	5.94
	IZO	2.80	1.16	2.00	VAC	1.10	2.28	1.62
	MLO	0.85	1.25	0.77	GIC	5.60	4.74	7.40
July 2014	HDP	5.99	37.37	2.92	KAS	4.29	17.57	7.17
	SPL	10.79	26.32	4.09	SSL	8.99	20.91	18.15
	NWR	5.17	18.78	3.71	JFJ	6.35	11.93	4.83
	SNP	29.28	48.33	12.88	PUY	7.23	13.29	12.80
	IZO	6.01	2.88	3.69	VAC	5.95	13.91	7.76
	MLO	1.47	1.68	1.31	GIC	20.30	15.36	28.58

Table 7. TCCON stations used for model evaluation, their location and reference

Site	Latitude	Longitude	Reference
Ascension Island	-7.92	-14.33	Feist et al. (2014)
Bialystok	53.23	23.02	Deutscher et al. (2015)
Bremen	53.10	8.85	Notholt et al. (2014)
Darwin	-12.43	130.93	Griffith et al. (2014a)
Edwards	34.96	-117.88	Iraci et al. (2016)
Garmisch	47.48	11.06	Sussmann and Rettinger (2015)
Izana	28.31	-16.48	Blumenstock et al. (2017)
Saga	33.24	130.29	Kawakami et al. (2014)
Karlsruhe	49.10	8.44	Hase et al. (2015)
Lauder	-45.04	169.68	Sherlock et al. (2014)
Lamont	36.60	-97.49	Wennberg et al. (2014b)
Orleans	47.97	2.11	Warneke et al. (2014)
Parkfalls	45.94	-90.27	Wennberg et al. (2014a)
Reunion Island	-20.90	55.49	De Mazière et al. (2014)
Rikubetsu	43.46	143.77	Morino et al. (2016b)
Sodankyla	67.37	26.63	Kivi et al. (2014)
Tsukuba	36.05	140.12	Morino et al. (2016a)
Wollongong	-34.41	150.88	Griffith et al. (2014b)

Table 8. Statistics for the average hourly XCO_2 and average daily XCO_2 comparison between TCCON measurements and MPAS-A simulations: RMS (ppm), bias (ppm), and correlation coefficient R. N is the number of data pairs used for computing of the statistics.

	Average hourly XCO_2				Average daily XCO_2			
Site	N	RMSE (ppm)	Bias (ppm)	R	N	RMSE (ppm)	Bias (ppm)	R
Ascension Island	1113	1.01	0.72	0.81	190	1.00	0.75	0.81
Bialystok	537	1.70	0.72	0.89	112	1.63	0.83	0.91
Bremen	222	2.30	1.04	0.85	51	2.20	1.15	0.87
Darwin	2109	1.18	0.85	0.68	296	1.06	0.79	0.77
Edwards	1515	1.01	0.57	0.90	257	0.91	0.57	0.93
Garmisch	567	1.10	0.18	0.91	99	1.14	0.20	0.91
Izana	210	0.51	0.24	0.94	56	0.51	0.26	0.94
Saga	516	0.97	0.30	0.91	107	0.95	0.29	0.91
Karlsruhe	522	1.99	0.92	0.85	93	1.73	1.05	0.88
Lauder	783	1.13	0.92	0.86	158	1.09	0.91	0.88
Lamont	1881	1.30	0.44	0.85	270	1.27	0.41	0.86
Orleans	573	2.06	0.95	0.75	114	1.84	1.01	0.81
Parkfalls	1200	1.35	0.17	0.93	194	1.27	0.15	0.94
Reunion Island	1092	1.03	0.86	0.91	186	1.00	0.86	0.93
Rikubetsu	180	1.26	-0.03	0.93	43	1.21	0.09	0.94
Sodankyla	243	1.33	0.83	0.97	54	1.26	0.85	0.97
Tsukuba	1086	1.55	0.26	0.80	169	1.42	0.22	0.82
Wollongong	1146	1.22	0.80	0.78	194	1.17	0.81	0.81

Table 9. The duration of four ACT aircraft campaign seasons

Campaign season	Duration
Summer 2016	Jul 15 to Aug 28
Winter 2017	Feb 01 to Mar 10
Fall 2017	Oct 01 to Nov 15
Spring 2018	Apr 12 to May 20

Table 10. Evaluation of MPAS simulated horizontal wind using radiosonde observations at 457 stations located across the globe. Wind speed and direction are compared at 00:00 UTC and 12:00 UTC at four pressure levels (1000 850, 500, and 200 hPa) for each day of the MPAS-A simulation. Note the number of data samples (N) is smaller at 1000 hPa because some stations are located above that pressure level.

	Pressure level	Mean RMSE vector wind (m/s)	Bias Wind speed(m/s)	Mean difference Wind direction °	N
Summer2016	1000 hPa	3.87	0.63	34.15	11,630
	850 hPa	3.75	-0.41	28.70	34,107
	500 hPa	3.58	-0.57	18.84	35,213
	200 hPa	4.58	-0.52	13.40	34,732
Winter2017	1000 hPa	4.02	1.01	32.00	11,415
	850 hPa	4.11	-0.32	25.28	27,957
	500 hPa	4.03	-0.43	14.67	28,977
	200 hPa	4.55	-0.48	9.79	28,401
Fall2017	1000 hPa	3.76	0.99	32.00	12,396
	850 hPa	4.05	-0.38	25.38	31,964
	500 hPa	3.92	-0.45	14.93	32,881
	200 hPa	4.63	-0.46	10.39	32,252
Spring2018	1000 hPa	3.98	0.89	33.80	10,763
	850 hPa	4.05	-0.30	27.85	29,886
	500 hPa	4.12	-0.42	17.24	30,914
	200 hPa	4.79	-0.46	12.96	30,257

Table 11. Comparison of mean CO_2 dry air mole fraction (ppm) in the boundary layer between the warm and the cold sectors. The table includes 10 frontal crossing flights from the Summer 2016 season and 5 from 2017 winter season. The column labeled as diff is the mean value of the warm sector minus that of the cold sector.

date	ACT			MPAS-A			WRF-Chem			CT2019		
yyyy-mm-dd	warm	cold	diff	warm	cold	diff	warm	cold	diff	warm	cold	diff
2016-07-18	396.7	396.7	0.0	396.7	402.1	-5.4	392.2	398.4	-6.2	397.8	399.1	-1.3
2016-07-19	398.2	396.6	1.6	404.9	393.5	11.4	400.2	394.3	5.9	399.6	397.9	1.7
2016-07-25	400.8	390.5	10.3	400.4	393.4	7.0	399.3	389.9	9.4	402.0	395.2	6.8
2016-07-26	405.9	396.1	9.8	419.4	394.8	24.6	424.8	394.0	30.8	408.4	396.3	12.1
2016-08-03	399.8	401.7	-1.9	401.7	398.4	3.3	400.8	401.1	-0.3	401.3	399.1	2.2
2016-08-04	407.3	393.5	13.8	408.2	391.3	16.9	407.5	399.8	7.7	403.0	390.7	12.3
2016-08-08	412.2	385.3	26.9	422.9	386.0	36.9	405.1	383.9	21.2	407.3	392.0	15.3
2016-08-12	401.4	395.1	6.3	404.4	392.1	12.3	405.4	402.8	2.6	399.6	395.3	4.3
2016-08-20	404.0	395.1	8.9	406.2	389.2	17.0	406.6	393.3	13.3	404.3	395.2	9.1
2016-08-21	406.5	390.7	15.8	408.1	387.0	21.1	414.8	392.5	22.3	404.1	394.1	10.0
2017-02-12	408.1	414.2	-6.1	409.7	412.1	-2.4	409.7	413.1	-3.4	408.3	410.9	-2.6
2017-02-17	413.5	414.8	-1.3	411.8	415.1	-3.3	411.5	413.2	-1.7	411.5	414.0	-2.5
2017-02-23	409.4	419.1	-9.7	411.7	417.6	-5.9	409.8	428.2	-18.4	409.6	415.0	-5.4
2017-03-07	412.0	415.2	-3.2	415.3	417.1	-1.8	417.4	418.4	-1.0	413.7	413.8	-0.1
2017-03-10	410.8	413.5	-2.7	413.5	415.3	-1.8	414.2	416.2	-2.0	412.3	413.4	-1.1

Table 12. Mean absolute error (MAE) of MPAS-A, WRF-Chem and CT2019 validated using ACT aircraft CO_2 measurements from four campaign seasons. p value of paired $t-$test between MPAS-A and the other two models given for each season to provides a significance level for the model comparisons.

		Mean Absolute Error			p-value of paired t test	
Season	Number of profiles	MPAS-A	WRF-Chem	CT2019	MPAS-A vs CT2019	MPAS-A vs WRF-Chem
Summer 2016	72	3.80	4.38	3.03	0.06	0.21
Winter 2017	27	1.56	2.23	1.58	0.95	0.09
Fall 2017	40	2.55	3.25	3.16	0.04	0.11
Spring 2018	60	2.29	3.75	1.99	0.23	0.01